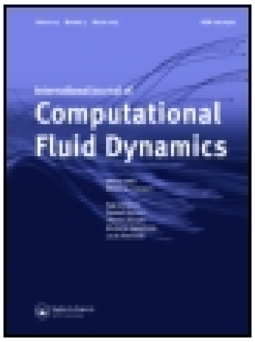

Taylor & Francis
Taylor & Francis Group

International Journal of Computational Fluid Dynamics

ISSN: 1061-8562 (Print) 1029-0257 (Online) Journal homepage: http://www.tandfonline.com/loi/gcfd20

GPU accelerated simulations of three-dimensional flow of power-law fluids in a driven cube

K. Jin, S.P. Vanka, R.K. Agarwal & B.G. Thomas

To cite this article: K. Jin, S.P. Vanka, R.K. Agarwal & B.G. Thomas (2017): GPU accelerated simulations of three-dimensional flow of power-law fluids in a driven cube, International Journal of Computational Fluid Dynamics, DOI: 10.1080/10618562.2016.1270449

To link to this article: http://dx.doi.org/10.1080/10618562.2016.1270449

INTERNATIONAL JOURNAL OF COMPUTATIONAL FLUID DYNAMICS, 2017
http://dx.doi.org/10.1080/10618562.2016.1270449

GPU accelerated simulations of three-dimensional flow of power-law fluids in a driven cube

K. Jin[a], S.P. Vanka[a], R.K. Agarwal[b] and B.G. Thomas[a,c]

[a]Department of Mechanical Science and Engineering, University of Illinois at Urbana-Champaign, Urbana, IL, USA; [b]Department of Mechanical Engineering and Materials Science, Washington University in St. Louis, St. Louis, MO, USA; [c]Department of Mechanical Engineering, Colorado School of Mines, Golden, CO, USA

ABSTRACT

Newtonian fluid flow in two- and three-dimensional cavities with a moving wall has been studied extensively in a number of previous works. However, relatively a fewer number of studies have considered the motion of non-Newtonian fluids such as shear thinning and shear thickening power law fluids. In this paper, we have simulated the three-dimensional, non-Newtonian flow of a power law fluid in a cubic cavity driven by shear from the top wall. We have used an in-house developed fractional step code, implemented on a Graphics Processor Unit. Three Reynolds numbers have been studied with power law index set to 0.5, 1.0 and 1.5. The flow patterns, viscosity distributions and velocity profiles are presented for Reynolds numbers of 100, 400 and 1000. All three Reynolds numbers are found to yield steady state flows. Tabulated values of velocity are given for the nine cases studied, including the Newtonian cases.

ARTICLE HISTORY
Received 3 June 2016
Accepted 5 December 2016

KEYWORDS
Non-Newtonian fluid; power-law fluid; three-dimensional cavity flow; GPU

1. Introduction

Shear flows in cavities generated by the motion of one or more bounding walls have been the subject of numerous studies (e.g. Ghia, Ghia, and Shin 1982; Gupta, Manohar, and Stephenson 1983; Peric, Kessler, and Scheuerer 1988; Kondo, Tosaka, and Nishimura 1991; Huser and Biringen 1992; Sundaresan et al. 1998; Aydin and Fenner 2001; Sahin and Owens 2003; Zhang 2003; Bruneau and Saad 2006; Pasquim and Mariani 2008; Heaton 2008; Kalita and Gupta 2010; Patil, Lakshmisha, and Rogg 2006; Bustamante et al. 2011; Guo et al. 2014; Backx and Wirz 1975; Freitas et al. 1985; Koseff and Street 1984; Ku, Hirsh, and Taylor 1987; Iwatsu et al. 1989; Huang et al. 1992; Arnal et al. 1992; Cantaloube and Le 1992; Deshpande and Shankar 1993; Jordan and Ragab 1994; Cortes and Miller 1994; Yeckel, Smith, and Derby 1997; Albensoeder, Kuhlmann, and Rath 2001; Guermond et al. 2002; Sheu and Tsai 2002; Albensoeder and Kuhlmann 2005; De, Nagendra, and Lakshmisha 2009; Yau, Badarudin, and Rubini 2012; Siegmann-Hegerfeld, Albensoeder, and Kuhlmann 2013; Tang et al. 2013; Dong et al. 2014; Verstappen et al. 1994; Deshpande and Milton 1998; Leriche, Gavrilakis, and Labrosse 2000; Paramane and Sharma 2008; De Vicente et al. 2011; Darr and Vanka 1991; Jyotsna and Vanka 1995; González et al. 2011; Jyotsna and Vanka 1996; Glowinski, Guidoboni, and Pan 2006; Shinn, Goodwin, and Vanka 2009; Bell and Surana 1994; Neofytou 2005; Yapici, Karasozen, and Uludag 2009; Grillet et al. 1999; Gao and Liu 2009; Haque et al. 2012; Mendu and Das 2012; Li et al. 2014). The widely studied case is the flow generated by the motion of the top wall of a square cavity in which a primary recirculating eddy and two smaller corner eddies at the bottom left and bottom right corners are generated. For Newtonian fluids, bench-mark solutions of two-dimensional (2D) flow in a square cavity have been published by several researchers (e.g. Ghia, Ghia, and Shin 1982; Gupta, Manohar, and Stephenson 1983; Peric, Kessler, and Scheuerer 1988; Kondo, Tosaka, and Nishimura 1991; Huser and Biringen 1992; Sundaresan et al. 1998; Aydin and Fenner 2001; Sahin and Owens 2003; Zhang 2003; Bruneau and Saad 2006). A number of studies for three-dimensional (3D) flow in a cube driven by the top wall have also been published (e.g. Backx and Wirz 1975; Freitas et al. 1985; Koseff and Street 1984; Ku, Hirsh, and Taylor 1987; Iwatsu et al. 1989; Huang et al. 1992; Arnal et al. 1992; Cantaloube and Le 1992; Deshpande and Shankar 1993; Jordan and Ragab 1994; Cortes and Miller 1994; Yeckel, Smith, and Derby 1997; Albensoeder, Kuhlmann, and Rath 2001; Guermond et al. 2002; Sheu and Tsai 2002; Albensoeder and Kuhlmann 2005; De, Nagendra, and Lakshmisha 2009; Yau, Badarudin, and Rubini 2012; Siegmann-Hegerfeld, Albensoeder, and

CONTACT S.P. Vanka ✉ spvanka@illinois.edu

Kuhlmann 2013; Tang et al. 2013; Dong et al. 2014; Verstappen et al. 1994; Deshpande and Milton 1998; Leriche, Gavrilakis, and Labrosse 2000), illustrating the rich 3D flow structures that are generated by the walls in the spanwise direction and by the instabilities of the curved streamlines. It is seen that on the bottom wall, streamwise vortical structures akin to Taylor-Göertler vortices are generated after a critical Reynolds number is exceeded. In addition, the flow becomes progressively more complex, eventually becoming unsteady and turbulent (Tang et al. 2013; Dong et al. 2014; Verstappen et al. 1994). The rectangular shape has been the most widely studied geometry, and has become a standard problem for development and validation of computational algorithms and codes. A smaller number of studies have been performed on cavities of other shapes, such as trapezoidal (Paramane and Sharma 2008; De Vicente et al. 2011; Darr and Vanka 1991), triangular (Paramane and Sharma 2008; Jyotsna and Vanka 1995; González et al. 2011), semi-circular (Jyotsna and Vanka 1996; Glowinski, Guidoboni, and Pan 2006) and other complex shapes (Shinn, Goodwin, and Vanka 2009). All these studies have assumed a Newtonian behaviour for the fluid with the viscosity assumed to be constant in the flow domain.

When the fluid behaves as non-Newtonian, the viscosity is no longer just a fluid property but also depends on the local strain rate. This brings additional nonlinearity to the flow, and consequent complexity to the computational algorithm. Locally, the strain rate can vary considerably because of the changes in the velocity field, such as in the driven cavity with multiple vortices. The fluid can be shear thickening or shear thinning, or may behave as a viscoplastic with a yield stress. Several nonlinear stress versus strain-rate relations have been published in literature, with the power-law variation being the most common for viscous non-Newtonian fluids.

There have been several studies reporting non-Newtonian flow in a 2D square cavity (e.g. Bell and Surana 1994; Neofytou 2005; Yapici, Karasozen, and Uludag 2009; Grillet et al. 1999; Gao and Liu 2009; Haque et al. 2012; Mendu and Das 2012; Li et al. 2014; Syrakos, Georgiou, and Alexandrou 2013; Prashant and Derksen 2011; Sanchez 1998; Mitsoulis and Zisis 2011; Vola, Boscardin, and Latché 2003; Elias, Martins, and Coutinho 2006) for power law fluids, and other types, including Bingham fluids. Bell and Surana (1994) computed the flow in the driven cavity using a p-version least-squares finite-element formulation (LSFEF) of 2D, incompressible, non-Newtonian fluid flow under isothermal and non-isothermal conditions. A power-law model for the non-Newtonian viscosity was used. Velocity profiles and streamlines for different values of the power law coefficient greater than and less than unity were presented. Neofytou (2005) developed a numerical method using QUICK (Leonard 1981) and the SIMPLE method (Patankar and Spalding 1972) for solving non-Newtonian viscous flows. The non-Newtonian models employed are the power law, Quemada, Bingham and Casson models appropriate for viscous and viscoplastic fluids. From the parametric study of the shear-thickening and shear-thinning effects on the flow it was observed that for both shear-thinning and shear-thickening fluids, increasing Reynolds number causes higher velocity gradients and subsequent moving of the centre of the main vortex towards the lid. The more shear-thinning the fluid is the closer is the centre of the main vortex to the upper right edge.

Yapici, Karasozen and Uludag (2009) used a collocated-grid finite volume method with the SIMPLE algorithm (Patankar and Spalding 1972) and momentum interpolation, to investigate the behaviour of a Oldroyd-B viscoelastic fluid (in this model the steady shear viscosity is Newtonian) in a 2D lid-driven cavity with the top wall moving in x direction. A non-uniform grid with 305×305 finite volumes was used. The convection and diffusion terms were discretised with second-order accuracy while first-order upwind scheme was used to calculate the viscoelastic stresses. They investigated the effect of Reynolds number ($Re = 0$, 100 and 400) and Weissenberg number (Wi from 0 to 1) and plotted Wi versus the centre of the main vortex for $Re = 100$ and 400. For a fixed Reynolds number, the magnitude of the minimum horizontal velocity on the vertical centreline decreased in its maximum magnitude with increase in the Weissenberg number. At low Reynolds numbers, the size of secondary eddies at the bottom corners decreased with increasing Wi, while at moderate Reynolds number (e.g. $Re = 400$) the two secondary vortices first increased with increasing Wi and merged into one big secondary vortex when $Wi = 0.3$. However, further increase in Wi made the vortices again separate and their size decreased. Values of the normal stress difference near the top wall are also presented.

Grillet et al. (1999) simulated the non-Newtonian Stokes flow in a square cavity at low Reynolds number, taking into account the resolution of the singularity at the two corners. Their approach of resolving the singularity was through a leakage flow at the top right and top left corners. The stresses were split in a primary component proportional to the strain rate, and an elastic component given by a polymer model. The Stokes equations were solved by a convergent and highly accurate mixed finite element technique. Their work was motivated by the desire to understand the viscoelastic instabilities in recirculation flows. The effects of polymer stresses on the flow kinematics and positions of the vortex centres and the effects of the geometric aspect ratio of the cavity were studied.

Gao and Liu (2009) developed a second-order accurate hybrid finite volume and finite element code, and applied it to study the incompressible non-Newtonian fluid flow in a 2D lid-driven cavity. The momentum equations were discretised by a cell-centred finite volume method while the pressure Poisson equation was discretised by a vertex-based finite element. The fractional step pressure projection was used to resolve the pressure-velocity coupling. The flows at Reynolds number of 100 for values of power-law index $n = 0.5$, 1.0 and 1.5 were computed. As the power law index n increased from 0.5 to 1.5, the main vortex centre was seen to shift from the top downstream corner towards the cavity centre. Also as n increased from 0.5 to 1.5, the size of the secondary vortex at downstream bottom corner increased considerably while the upstream bottom eddy increased only slightly. They also observed that the horizontal velocity on the vertical centreline for $n = 0.5$ is much smaller than that of $n = 1.5$.

Haque et al. (2012) studied the conditions for stability of flow of a non-Newtonian fluid in a 2D lid-driven cavity. The viscosity was modelled by the Carreau model and the flow in square and shallow cavities of aspect ratio of 0.25 were modelled. They presented results for various power indices from 0.4 to 1.4 and a time constant $\lambda = 1$, 10 and 100. A base flow solution was first obtained by solving the discretised continuity and momentum equations using Newton–Raphson iterations. The solutions were then substituted into a perturbation equation and the stability behaviour was studied. In general, shear-thickening effects were seen to stabilise the flow, while shear-thinning created instabilities at lower Reynolds numbers. At the lowest values of n considered, the critical Reynolds number increased again. Further, an intermediate range of values of the power index n at which the instability mechanism is unaffected by non-Newtonian effects was observed.

Mendu and Das (2012) used the Bhatnagar–Gross–Krook (BGK) single-time approximation (Bhatnagar, Gross, and Krook 1954) Lattice Boltzmann Method (LBM) to study the flow of a power-law fluid in a driven cavity with both top and bottom walls moving. They studied different configurations by setting the two walls moving in the same or in the opposite direction with different velocities. A 257 × 257 lattice grid was used and combinations of three values of the power-law index n (0.5, 1.0 and 1.5) and three Reynolds numbers (100, 400 and 1000) were computed. Centreline velocities as well as the locations of the vortex centres are reported. The drag coefficient of the moving lid was found to increase with increasing n, but was not sensitive to the moving directions of the two lids. For parallel walls moving at a fixed Reynolds number, the two main vortices moved towards the centre of the cavity with increasing value of the index n. For anti-parallel wall motion with $n = 1$ and $Re = 1000$, two small secondary vortices were observed at the two corners close to the stationary walls; however, the tendency of forming these secondary vortices decreased with increasing value of the power law index. Recently, Li et al. (2014) used a Multi-Relaxation-Time (MRT) LBM method with D2Q9 model to study the flow of a power law fluid in a 2D lid-driven cavity using a grid size of 256 × 256 lattice points. Reynolds numbers from 100 to 10000 and power-law index from 0.25 to 1.75 were considered. Streamlines, velocities on horizontal and vertical centre lines and vortex centres are presented for all the cases. The value of the primary stream function increased with Re for Re less than 3500 but decreased at higher Reynolds numbers. For a fixed power-law index close to one, the flow structures with power-law fluids were seen to be similar to those for a Newtonian fluid. However, noticeable differences between the flow structures with power-law fluids and of a Newtonian fluid were observed for other cases. For a fixed Reynolds number, the power-law index showed a significant influence on the number and the strength of vortices in the cavity.

Syrakos, Georgiou, and Alexandrou (2013) solved the creeping flow of a Bingham plastic fluid in a lid-driven cavity using the Papanastasiou regularization (Papanastasiou 1987) and the finite volume method combined with a multigrid algorithm. Results are presented for Bingham numbers in the range 0–1000. Their results compare favourably with the results of finite-element and the finite-difference methods. The convergence was accelerated considerably with a multigrid algorithm. The lid-driven cavity flow has also been used as a test case for Bingham flows by Prashant and Derksen (2011); Sanchez (1998); Mitsoulis and Zisis (2011); Vola, Boscardin, and Latché (2003); Elias, Martins, and Coutinho (2006), amongst others.

The 3D flow of a Newtonian fluid in a driven cavity (cube) driven by the top wall has also been the subject of a large number of numerical studies. Interest in such studies dates back to 1975 (Backx and Wirz 1975), and has been maintained steadily for the past 40 years. (References (Backx and Wirz 1975; Freitas et al. 1985; Koseff and Street 1984; Ku, Hirsh, and Taylor 1987; Iwatsu et al. 1989; Huang et al. 1992; Arnal et al. 1992; Cantaloube and Le 1992; Deshpande and Shankar 1993; Jordan and Ragab 1994; Cortes and Miller 1994; Yeckel, Smith, and Derby 1997; Albensoeder, Kuhlmann, and Rath 2001; Guermond et al. 2002; Sheu and Tsai 2002; Albensoeder and Kuhlmann 2005; De, Nagendra, and Lakshmisha 2009; Yau, Badarudin, and Rubini 2012;

Siegmann-Hegerfeld, Albensoeder, and Kuhlmann 2013; Tang et al. 2013; Dong et al. 2014; Verstappen et al. 1994; Deshpande and Milton 1998; Leriche, Gavrilakis, and Labrosse 2000) are selected to cite some relevant works on 3D flow in a cube.) There have been a variety of techniques used to compute essentially the same flow, albeit with different accuracy, grid, and Reynolds numbers. Finite volume methods (Freitas et al. 1985; Koseff and Street 1984; Iwatsu et al. 1989; Jordan and Ragab 1994), finite-element methods (Yeckel, Smith, and Derby 1997; Guermond et al. 2002), spectral methods (Ku, Hirsh, and Taylor 1987; Albensoeder, Kuhlmann, and Rath 2001; Albensoeder and Kuhlmann 2005), velocity vorticity methods (Huang et al. 1992) and Lattice Boltzmann methods (De, Nagendra, and Lakshmisha 2009; Tang et al. 2013; Dong et al. 2014) have been used. The primary features observed are nearly the same in all these studies. At low Reynolds numbers, the flow is similar to the flow in a 2D cavity, except for the boundary layers on the spanwise walls (if the spanwise direction is periodic, exactly 2D solutions are obtained). The central plane consists of a primary eddy and two secondary eddies in the right bottom and bottom left corners. One unique feature of 3D analyses is the capture of 3D structures even in a nominally 2D (i.e. periodic) geometry. At reasonably high Reynolds numbers, it has been observed that the recirculating primary eddy generates centrifugal instabilities (Albensoeder, Kuhlmann, and Rath 2001), and Taylor-Göertler-like (TGL) vortices are formed near the bottom walls (Guermond et al. 2002). Freitas et al. (1985) have applied a finite volume code REBUFFS to study the lid-driven 3D cavity flow at $Re = 3200$ and compared simulation results with their previous experiments. They used a $32 \times 32 \times 45$ grid and the SIMPLE algorithm with QUICK scheme and solved only half of the cavity by assuming the flow to be symmetric about the middle plane. They were able to capture the TGL vortices also found in the experiments. The size and the location of those vortices were observed to be time dependent. Mean velocities on the central lines of the symmetry plane were satisfactorily compared with Laser Doppler Velocity (LDV) measurements at $\mathrm{Re} = 3300$.

Jordan and Ragab (Jordan and Ragab 1994) studied the unsteady Newtonian flow in a cavity with 3:1 spanwise aspect ratio for Reynolds numbers of 5000, 7500 and 10000. For the largest Reynolds number, a subgrid scale model was used for the unresolved scales of turbulence. The LES results were also compared with experiments, and good agreement was obtained. A GAMM conference on 3D unsteady viscous flows was conducted in 1992, with one of the candidate problems being the flow in a driven cube. Arnal et al. (1992) studied the unsteady flow in a cube at $Re = 3200$ using a finite volume multigrid method on a co-located grid. The spatial resolution was found to be much more important than the temporal resolution in determining the instantaneous flow field. The grid used was coarse ($32 \times 32 \times 96$) for the full cavity. Iwatsu et al. (1989) used a 3D numerical technique to integrate the time-dependent Navier-Stokes equations. The 3D flow structure is presented in detail for several Reynolds numbers. It was found that the flow is steady at low Reynolds numbers, but becomes unsteady past $Re = 2000$. Due to the end walls, the flow was seen to be 3D even at low Reynolds numbers, with the appearance of Taylor-Goertler vortices at high Reynolds numbers.

Recently, Siegmann-Hegerfeld, Albensoeder, and Kuhlmann (2013) conducted an experimental and numerical investigation of the 3D flow in a cavity of width-to-height ratio of 1.6, with a span ratio of 10.85. Increasing the Reynolds number gradually led to the onset of 3D motion in a continuous manner, compared with the predictions of a sudden onset of three-dimensionality. This was explained as a consequence of the ubiquitous spanwise walls. A good agreement between experiments and numerical simulations was obtained.

In addition to the solution of the continuum-based Navier-Stokes equations, the mesoscopic approach of the LBM has also been used to study 3D flow in a cube. The findings on the flow are nearly the same as those from the continuum method. We refer to works by De, Nagendra, and Lakshmisha (2009), Tang et al. (2013) and Dong et al. (2014), who used multi-relaxation time and single-relaxation time LBM. The LBM simulations compared well with the Navier-Stokes solutions. The LBM method is an explicit, highly parallel method and does not involve any solution of pressure equation as in other algorithms. Tang et al. (2013) combined the LBM with a curvilinear coordinate and used both physical and computational spaces to predict the 3D flow.

Several other works have also studied the flow in a driven cube. Guermond et al. (2002) studied the impulsively started 3D flow in a 1:1:2 cavity at a Reynolds number of 1000. The initial evolution of the flow was computed as well as measured, and was found to be sensitive to the initial perturbations. Three-different ways of starting the motion of the top wall were studied experimentally and results were reproduced by the numerical simulations. Sheu and Tsai (2002) used a finite-element-based procedure with tri-quadratic elements and a mixed formulation. The linear equations were solved with BICGSTAB solver, and upstream biased formulation was used for achieving stability. The spiralling motion in the spanwise direction was characterised in detail.

When the flow Reynolds number is high, the unsteady flow in the cube becomes chaotic and eventually turbulent. Several researchers have measured and computed the turbulent flow in a driven cavity. Koseff and Street (1984) made measurements in a cavity of spanwise distance in a cavity of span three times the height and at a Reynolds number of 10,000. The flow visualization was accomplished using thymol blue technique and the velocities were measured using LDV. The flow was observed to consist of 3D features, corner eddies and Taylor-Goertler-like vortices. Deshpande and Milton (1998) simulated two Reynolds numbers ($Re = 3200$ and 10,000) resolving all the turbulence scales. The grid used had $84 \times 84 \times 84$ nodes. The velocity and dissipation spectra were used to compute the Kolmogorov scales in the flow. The Kolmogorov scales in the central core were observed to attain larger values in the central core compared with those in the top wall region. Verstappen et al. (1994) performed direct numerical simulation (DNS) of the 3D flow in a cube at $Re = 3200$ and $Re = 10{,}000$. Different spatial discretization schemes were tested and results were seen to reproduce the experimentally observed Taylor-Göertler-like vortices. A similar DNS was performed by Leriche, Gavrilakis, and Labrosse (2000) using a Chebyshev spectral method. The procedure was implemented on a 16-processor NEC machine and high-resolution DNS were performed. The same features observed in other investigations were also seen.

From the above literature survey, we observe that except for an isolated study of power-law fluid on a coarse grid (Reddy and Reddy 1992) and a study of Bingham plastic fluid of $Re = 1$ and 1000 (Elias, Martins, and Coutinho 2006) there have been no systematic studies of the 3D non-Newtonian flow in a cubical enclosure driven by the top wall motion. Three-dimensional flows are obviously much more computationally intensive, and require considerably more resources of both storage and CPU time. We are not aware of any studies with fine enough grids that have reported bench-mark quality velocity profiles which can be used for future comparisons. Fortunately, with the development of powerful parallel computers, it is now possible to perform large-scale, 3D flow calculations in reasonable computing times. One such parallel computing platform available on desktops to most users is the Graphical Processing Unit (GPU). In recent years, it has been increasingly recognised that the data parallel features of a GPU can be effectively exploited to perform large-scale scientific computations to achieve greater speeds. Recently, a considerable amount of interest has been generated for the use of the GPU as a data parallel computing platform. A recent review of implementation of computational fluid dynamics codes on GPUs has been given in Kirk and Hwu (2012), which refers to a large numbers of papers. In the past 10 years, many researchers have developed/ported CFD software to GPUs and found significant speed-ups (10–50 times depending on algorithm, approach and implementation) over a single core CPU. The GPU is a highly parallel, multi-threaded, many-core processor with a large computational horse power and high memory bandwidth. Each GPU consists of many streaming multiprocessors (SMPs). Thus, GPUs offer promise of a super computer (in a single box) with theoretical computing speed of a couple of Teraflops.

In this paper, we describe the application of a 3D Navier-Stokes solver implemented on a GPU (Sanders and Kandrot 2010; NVIDIA 2011) to compute generalised Newtonian fluid flows. The solver employs the well-known Harlow-Welch fractional step algorithm (Vanka 2013) for discretization of the governing equations. A considerable speedup is obtained between the CPU and the GPU, depending on the size of the problem; the bigger the size of the problem, the greater is the speedup. In this paper, this GPU-based computer code is applied to perform fine grid computations of the steady-state flow at moderate Reynolds numbers for two values of the power-law index. The results are presented in terms of streamline patterns and velocity profiles at the centre lines. Tables of the velocity data at selected lines are given.

2. Governing equations and numerical method

2.1. Governing equations

The governing equations for a steady incompressible flow in the absence of body forces can be written as:

$$\nabla \cdot \left(\rho \vec{u}\right) = 0 \tag{1}$$

$$\rho \left[\frac{\partial \vec{u}}{\partial t} + \left(\vec{u} \cdot \nabla\right) \vec{u} \right] = -\nabla p + \nabla \cdot \underline{\underline{\tau}} \tag{2}$$

Where $\underline{\underline{\tau}}$ is the deviatoric part of the Cauchy stress tensor, ρ is density, p is pressure and $\vec{u} = u_i \hat{e}_i$ is the velocity vector in the Cartesian system. The governing Equations (1) and (2) are solved for a constant density flow in a unit cube with top wall moving at a constant velocity $u_1 = U = 1$ m/s in x direction as shown in Figure 1. At all other walls, the velocities are zero and no-slip conditions are applied.

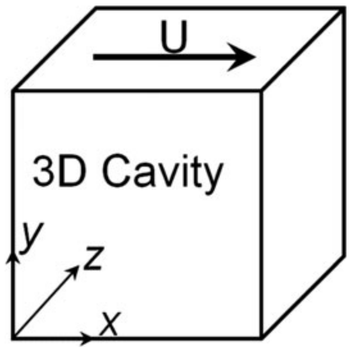

Figure 1. Geometry of the lid-driven cubic cavity.

2.2. Power-law model

In this paper, we have modelled the non-Newtonian fluid by a power law model. The deviatoric part of the Cauchy stress tensor $\underline{\underline{\tau}}$ is written as:

$$\underline{\underline{\tau}} = 2\mu\underline{\underline{\varepsilon}} \tag{3}$$

where μ is the effective dynamic viscosity and $\underline{\underline{\varepsilon}}$ is strain rate tensor defined as:

$$\varepsilon_{ij} = \frac{1}{2}\left(\frac{\partial u_i}{\partial x_j} + \frac{\partial u_j}{\partial x_i}\right) \tag{4}$$

In the power-law model, the effective viscosity is given by the following expression:

$$\mu = \mu_0|\dot{\varepsilon}|^{n-1} = \mu_0\left|\sqrt{2\varepsilon_{ij}\varepsilon_{ij}}\right|^{n-1} = \mu_0\left|2\varepsilon_{ij}\varepsilon_{ij}\right|^{\frac{n-1}{2}} \tag{5}$$

where μ_0 is the consistency index and n is the flow behaviour index of the non-Newtonian fluid. $n = 1$ corresponds to a Newtonian fluid, while $n > 1$ and $n < 1$ represent shear-thickening and shear-thinning fluids, respectively. For a power-law model and the driven cavity flow, the Reynolds number can be defined as

$$\begin{aligned}\mathrm{Re} &= \frac{\rho UL}{\mu} = \frac{\rho UL}{\mu_0\left|2\varepsilon_{ij}\varepsilon_{ij}\right|^{\frac{n-1}{2}}} \\ &= \frac{\rho UL}{\mu_0\left[2\left(\frac{1}{2}\frac{\partial u}{\partial y}\right)^2 + 2\left(\frac{1}{2}\frac{\partial u}{\partial y}\right)^2\right]^{\frac{n-1}{2}}} = \frac{\rho U^{2-n}L^n}{\mu_0}\end{aligned} \tag{6}$$

where U is the lid velocity and L is the representative dimension of the cavity. We have also non-dimensionalised all variables in Equations (1) and (2) and thus consider the flow in a cube of unit dimensions and unity top wall velocity.

2.3. Numerical method

An in-house code, CUFLOW (Vanka, Shinn, and Sahu 2011; Shinn 2011; Chaudhary 2011), that was recently developed to solve the governing Equations (1) and (2) for a Newtonian fluid was modified to include non-Newtonian relations in the form of a generalised Newtonian fluid. CUFLOW is a general purpose code for simulating laminar and turbulent flows in complex domains. CUFLOW employs Cartesian grids combined with the immersed boundary method to integrate the 3D unsteady incompressible Navier-Stokes equations. The fractional step method is employed to solve the continuity and momentum equations. We provide below brief details of the algorithm. Complete details are available in Shinn (2011) and Chaudhary (2011).

The velocities are first determined by solving the momentum Equations (2) without the pressure gradient terms. The discretised equations are derived in the finite-volume framework by central differencing both the convection and diffusion terms on a collocated grid. For the temporal differencing, the second-order accurate Adams-Bashforth scheme is used. Therefore, in the first-step, the discretised equations in the absence of pressure gradient terms become:

$$\rho\left(\frac{\hat{u}_i - {u_i}^r}{\Delta t}\right) = \frac{3}{2}H^r_{u_i} - \frac{1}{2}H^{r-1}_{u_i} \tag{7}$$

In the next step, the continuity equation is transformed to a pressure-Poisson equation given by

$$\frac{\rho}{\Delta t}\frac{\partial \hat{u}_i}{\partial x_i} = \frac{\partial}{\partial x_i}\left(\frac{\partial p}{\partial x_i}\right)^{r+1} \tag{8}$$

Equation (8) for pressure is solved efficiently by a V-cycle multi-grid method, and red-black Gauss-Seidel SOR (with over-relaxation parameter of 1.6). After computing the solution for pressure at $r + 1$ time step from Equation (8), the velocity components at $r + 1$ time step are computed using the pressure field. For steady state calculations, the algorithm is marched in time until desired convergence to steady state is achieved. In the current version of CUFLOW, an unstructured one-dimensional (1D) data structure is employed in order to simulate a complex geometry. CUFLOW has been successfully used to perform LES/DNS of turbulence in circular and triangular ducts, to calculate the effects of a micro ramp on the film cooling effectiveness (Shinn 2011), and to compute the flow and heat transfer in the mould region of an actual continuous caster of steel in the presence of a magnetic field (Chaudhary 2011). In the present study, CUFLOW has been extended to non-Newtonian fluids and calculations for power-law fluids in the lid-driven cube of Figure 1 have been conducted.

2.4. GPU implementation

The above algorithm has been programmed to run entirely on a GPU. The Nvidia Tesla K20x GPU has been observed to provide a factor upwards of eighteen speed up over serial execution on an 8 core Intel Xeon E5-2650v2 2.6 GHz CPU. GPU programming can be done in several different languages such as OpenCL, CUDA and OpenGL. Of these, OpenCL and CUDA are most commonly used. We have implemented the algorithm in CUDA Fortran. CUDA Fortran is supported by the PGI Fortran compiler when the filename uses a .cuf extension. The grid generation, initial conditions and boundary conditions are first created on CPU and data are then copied to GPU. For each computational step, a separate GPU kernel is launched. The flow fields from the GPU are copied periodically to the CPU for plotting and interrogation. The variables are all stored as 1D arrays. The GPU launches data in blocks of pre-specified sizes and each block is assigned to one SMP. The SMP launches threads which are then assigned to kernels. A kernel is a set of instructions assigned to one thread to be executed independent of other data. Thus, GPU is a data parallel computer, operating same instructions in parallel on multiple data. As mentioned earlier, CUFLOW uses an explicit algorithm for momentum equations and a red-black SOR algorithm for the pressure-Poisson equation. Both these are data parallel algorithms and easily map to a GPU. As a result we have observed a gain in computational speed upwards of 18 over serial running on an Intel Xeon E5-2650v2 2.6-GHz CPU.

3. Code validation

CUFLOW has been previously validated in a number of flow problems, including DNS of turbulent flow in square ducts, MHD flow in channels and rectangular ducts (Chaudhary 2011), continuous casting of steel, and in film cooling flows with vortex generators (Shinn 2011). The current version of CUFLOW uses a collocated grid (versus a staggered grid), and hence was validated again for flow in a driven cube with a Newtonian fluid against previous simulations and simulations of Ku, Hirsh, and Taylor (1987). Figure 2 shows the comparison of the velocity profiles at mid-span along horizontal and vertical lines. The solution of Ku et al. was obtained with a spectral technique and our simulations were performed with a 128 × 128 × 128 uniform finite volume grid. Several coarser grids were also computed, but the 128 × 128 × 128 grid was used in all simulations to get high accuracy. Since the code used a GPU, the computations were quite fast and did not require much GPU time. The calculations were performed by marching in time to steady state, and a steady state was judged by successive changes of velocities to be less than 1.0×10^{-5} for a nominal value of 1.0.

To validate the incorporation of the non-Newtonian viscosity and stress terms, we computed the 2D driven cavity flow of a power law fluid using the 3D code for a rectangular parallelepiped with aspect ratio 1:1:8. The

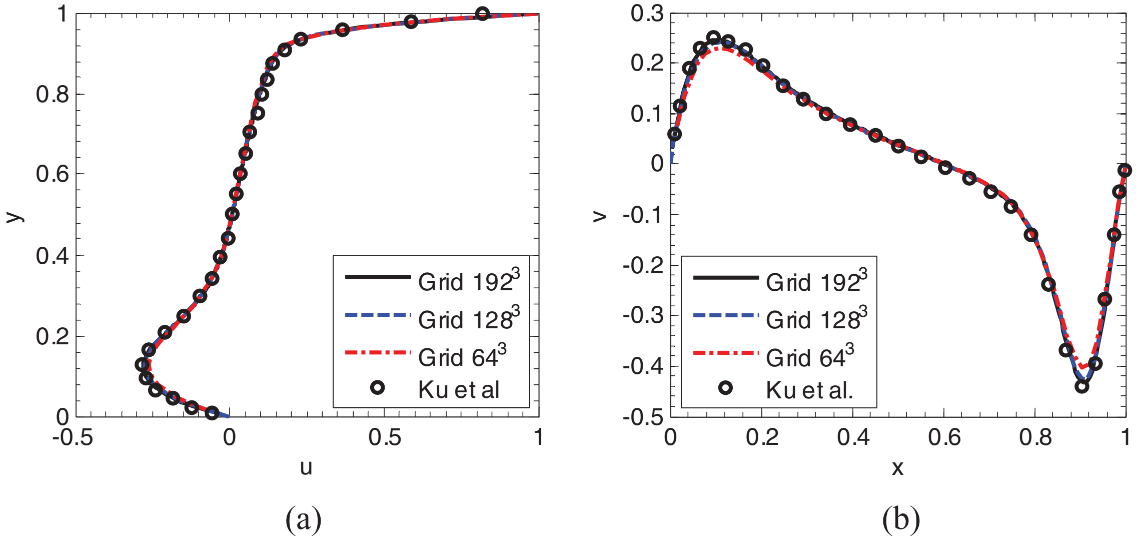

(a) (b)

Figure 2. Comparison of velocity profiles in a lid-driven cube, $Re = 1000$ with Ku, Hirsh, and Taylor (1987). (a) x-velocity along vertical centreline. (b) y-velocity along horizontal centreline.

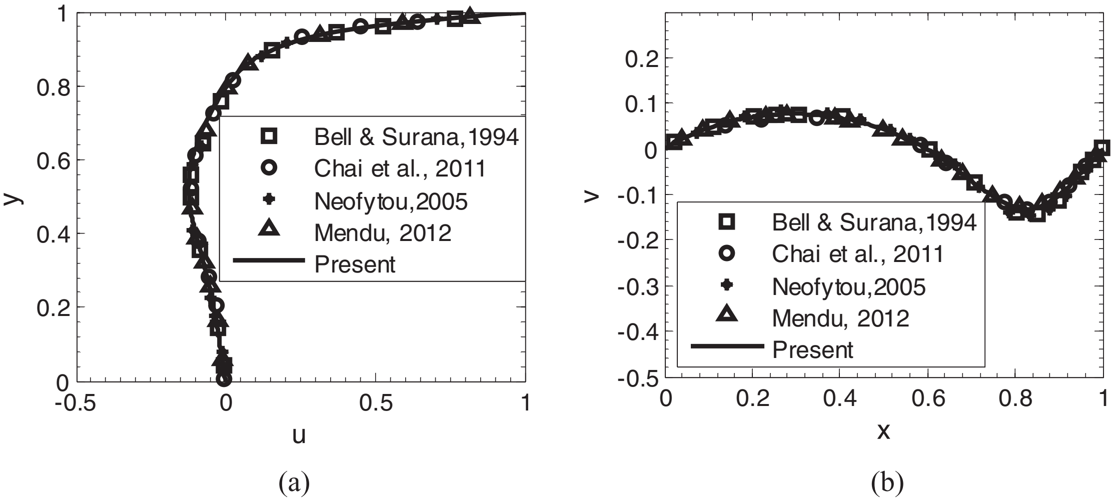

Figure 3. Horizontal and vertical velocity profiles in the mid-span plane, compared with 2D results of non-Newtonian flow in a driven cavity. (a) Velocity along the vertical centreline. (b) Velocity along the horizontal centreline.

results on the symmetry plane ($z = 4$), far from the solid boundary, are compared with existing 2D results from the literature. The flow Reynolds number is 100 and power-law index is 0.5 which corresponds to a shear thinning fluid. A uniform grid of $128 \times 128 \times 512$ in (x, y, z) directions is employed with an element size of $\Delta z = 2\Delta x = 2\Delta y$. In Figure 3, the x-direction velocity profile on the vertical centreline and y-direction velocity profile on the horizontal centreline of symmetry surface are plotted against the 2D simulation results of other investigators. The 2D results shown in Figure 3 include the results obtained by a variety of algorithms. Bell and Surana (1994) employed the finite element method, Neofytou (2005) used the finite volume method, and Li et al. (2014) and Mendu (Mendu and Das 2012) applied the Lattice Boltzmann Method (LBM). The excellent agreement among all the calculations validates the accuracy of non-Newtonian version of the CUFLOW code.

4. Results and discussion

In the present work, flow at three different Reynolds numbers ($Re = 100$, 400 and 1000) was investigated. The different Reynolds numbers were obtained by modifying the consistency indexμ_0. The computed effective viscosity μ is trapped between $0.1\mu_0$ and $10\mu_0$. For each Reynolds number, three values of the non-Newtonian flow behaviour index were used ($n = 0.5$, 1.0 and 1.5) that represent shear-thinning, Newtonian and shear-thickening behaviours, respectively. The flow structure, velocity distribution and velocity values for these nine simulations are presented below.

4.1. $Re = 100$

As shown in Equation (7), to obtain $Re = 100$ with fixed fluid density, top wall shear velocity and domain length, the consistency index μ_0 was set to be 0.01. For the Newtonian fluid case ($n = 1$) the fluid dynamic viscosity was a constant and equals the consistency index. However, for the shear-thinning and shear-thickening fluids, the local effective viscosity varies considerably as a result of local strain rates tensor. The flow was found to be steady and a converged flow distribution was obtained by marching in time. Figure 4 shows streamlines and contours of viscosity for the shear-thinning case ($n = 0.5$) at different z planes. In these figures, we observe one large eddy centred at a region close to the right side of the top moving wall. In the bottom two corners of the cavity, minor vortices may be present in very small regions below the grid resolution used here ($\Delta x = \Delta y = 1/128$) but are not captured in these simulations. High-viscosity regions are observed close to the bottom front and back edges due to the slow motion of the fluid. In addition, Figure 6(d)–(f) show that at region $(x, y) \approx (0.3, 0.8)$ a relatively high viscosity spot ($\mu = 0.04$–0.05) is formed locally, indicating that there exists a local low shear region. It is also noticeable that in the bottom corner a high viscosity triangular region is formed and is larger close to the side walls, shrinking as we move towards the centre plane (z = 0.5). The size of the region is almost the same for planes that are 0.2 away from the side wall to the middle plane ($z = 0.5$). The vertical side of the high viscosity triangular region (viscosity greater than 0.09) shrinks from ~0.2 to ~0.1 as we move from $z = 0.05$ to $z = 0.5$.

Figure 5 presents contours of viscosity and streamlines at different z planes for the shear-thickening case.

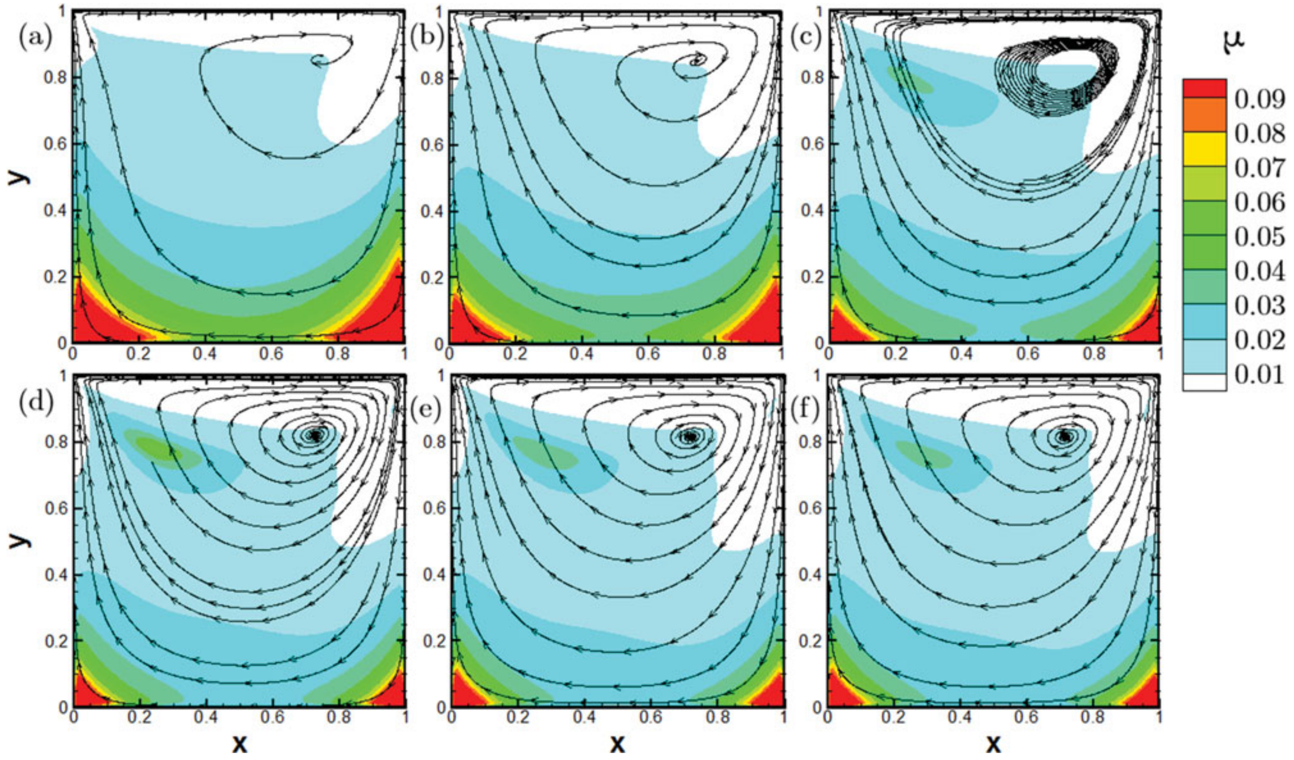

Figure 4. Contours of viscosity and streamlines at different z planes: (a) $z = 0.05$; (b) $z = 0.1$; (c) $z = 0.2$; (d) $z = 0.3$; (e) $z = 0.4$; (f) $z = 0.5$ for $Re = 100$ and $n = 0.5$.

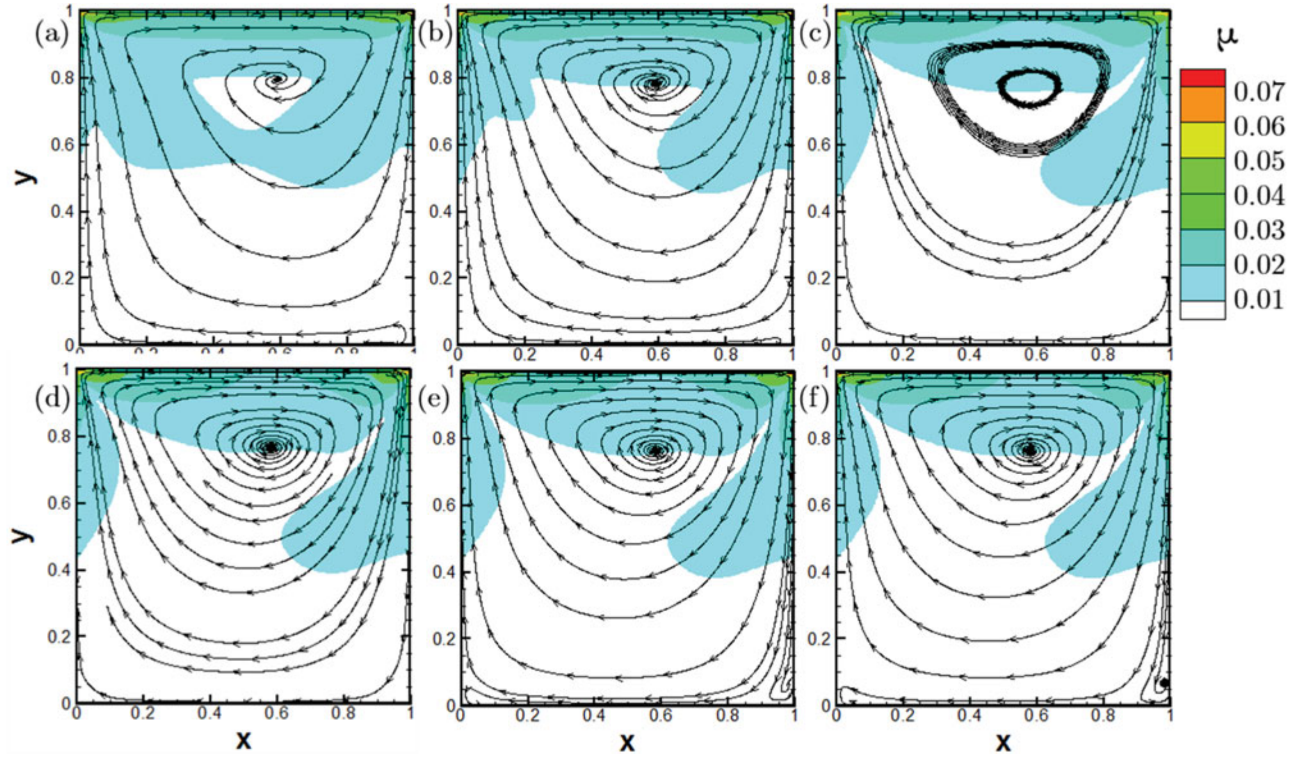

Figure 5. Contours of viscosity and streamlines at different z planes: (a) $z = 0.05$; (b) $z = 0.1$; (c) $z = 0.2$; (d) $z = 0.3$; (e) $z = 0.4$; (f) $z = 0.5$ for $Re = 100$ and $n = 1.5$.

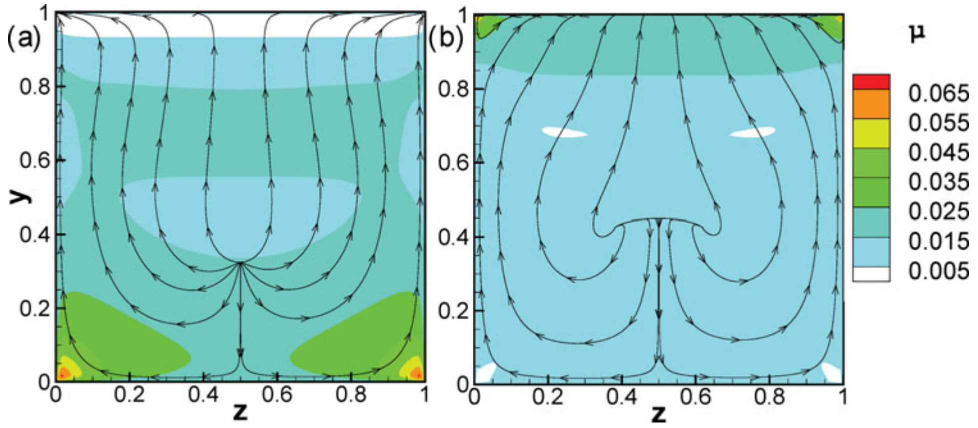

Figure 6. Contour plots of viscosity and streamlines in spanwise plane $x = 0.5$ for $n = 0.5$ (left) and $n = 1.5$ (right), $Re = 100$.

The corresponding viscosity contours indicate that for a shear-thickening fluid the effective viscosity in much of the cavity is below 0.02 which is two times the consistency index. Very high viscosity regions were found at the top front and back edges due to the high shear (not seen in the figure due to small region close the corner). The streamlines show that in contrast to the shear-thinning case, two very small eddies are formed at the two bottom corners at middle plane. Locally low viscosity ($\mu < 0.01$) regions are found close to all the eddy centres, and the effective viscosity of the fluid in the bottom half ($y < 0.5$) of the cavity is lower than the consistency index μ_0.

Figure 6(a) and (b) show contour plots of viscosity and streamlines in the plane at $x = 0.5$ for $n = 0.5$ and $n = 1.5$, respectively. For $n = 0.5$, the results show that the low viscosity regions are close to the top moving wall ($y = 1$). The streamlines on the middle x plane for the shear-thickening fluid ($n = 1.5$) are shown in Figure 6(b). Both figures indicate that the flow at the side walls is moving upwards. The viscosity contours for the shear-thickening fluid indicate that the low viscosity region is relatively in the bottom part of the cavity and high viscosity region is close to the top moving wall, as expected from the computed shear pattern.

The computed relative viscosity μ/μ_0 on horizontal and vertical centrelines of the symmetry plane is plotted in Figure 7 (a) and (b), respectively. On the horizontal centreline, the viscosity variation for shear thickening fluid $n = 1.5$ is not very large and the maximum viscosity happens at close to the downstream wall. Moving from upstream wall towards the downstream wall, the relative viscosity ratio first drops from 1.1 to 0.9 and then increases to around 1.2 at the region close to the downstream wall where shear rate is higher. However, for the shear thinning fluid the maximum high relative viscosity region ($\mu/\mu_0 = 1.6$) is seen close to the left wall, then it drops as we move towards the right wall, reaching its minimum value at $x = 0.85$. It rises to around 1.1 in the region close to the wall. The relative viscosity on the vertical centreline for case $n = 0.5$ indicates that as we traverse downward from the top wall ($y = 1.0$) the relative viscosity first increases from 0.5 to 2.0, and reaches

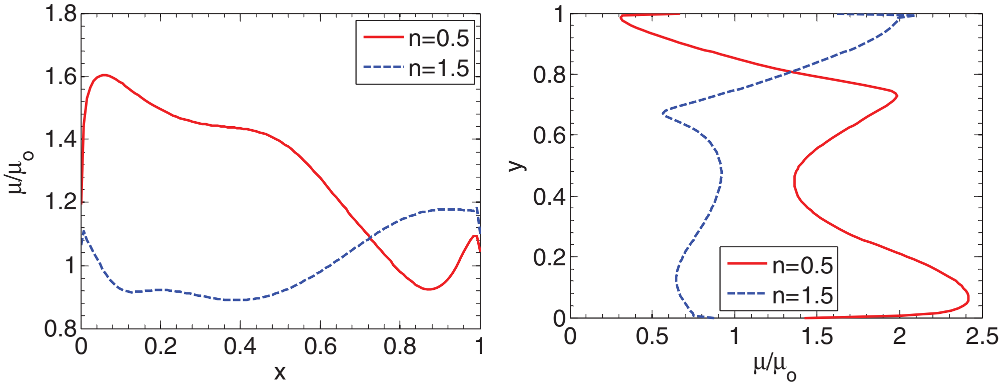

Figure 7. Relative viscosity variation on horizontal (left) and vertical (right) centrelines for $n = 0.5$ and $n = 1.5$, $Re = 100$.

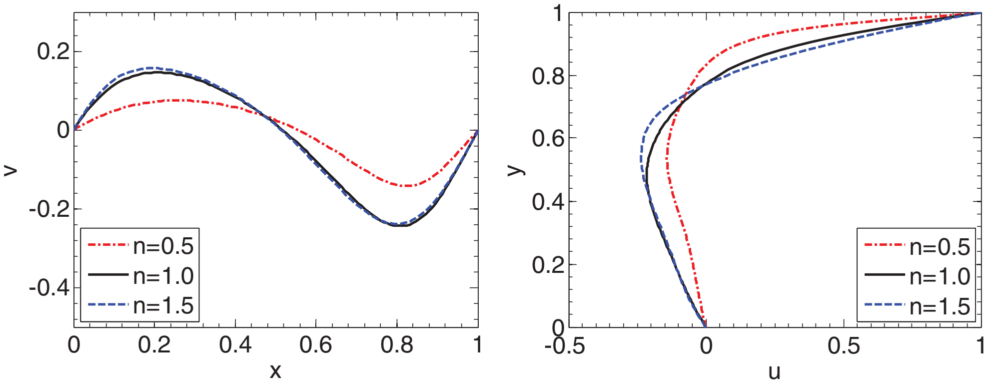

Figure 8. *v* velocity on horizontal centreline (left) and *u* velocity on vertical centreline (right) for *Re* = 100.

the maximum value at $y = 0.75$ and then it decreases to 1.3 at $y = 0.45$, and after that it increases again to 2.4 at $y = 0.05$. For $n = 1.5$, as we move from $y = 1.0$ to $y = 0.7$, the relative viscosity decreases from 2.2 to 0.5, but slowly increases and then decreases to another local minimum value of 0.6 at $y = 0.1$. After that, moving down the cavity the viscosity increases again.

The v velocity on horizontal centre line and u velocity on vertical centreline for different fluids are plotted in Figure 8(a) and (b), respectively. The v velocity on horizontal centreline shows that the peak v velocity increases as n increases from 0.5 to 1.5, and the maximum v velocity for the Newtonian and shear-thickening fluids can be twice that with $n = 0.5$. The minimum v velocity for shear-thickening fluid can also be twice that of the shear-thinning fluid. For the u velocity on the vertical centreline, the results also show that the magnitude of the peak negative u velocity for $n = 1.5$ is slightly higher than that of the Newtonian fluid but twice the value for shear-thinning fluid with $n = 0.5$. The boundary layer for the shear-thinning fluid is thinner at the top wall. Selected points on Figure 8 are tabulated in Table 1. These values can be used by others for their code validation and benchmarking.

Table 1. *v* velocity on horizontal centreline and *u* velocity on vertical centreline at *Re* = 100.

v velocity on horizontal centreline			
X	*n* = 0.5	*n* = 1.0	*n* = 1.5
0.1	4.94E-02	1.14E-01	1.28E-01
0.2	7.26E-02	1.47E-01	1.57E-01
0.3	7.41E-02	1.30E-01	1.36E-01
0.4	5.79E-02	8.46E-02	8.79E-02
0.5	2.58E-02	1.50E-02	1.31E-02
0.6	−2.38E-02	−7.75E-02	−8.60E-02
0.7	−8.82E-02	−1.81E-01	−1.88E-01
0.8	−1.39E-01	−2.43E-01	−2.38E-01
0.9	−1.09E-01	−1.79E-01	−1.72E-01
u velocity on vertical centreline			
y	*n* = 0.5	*n* = 1.0	*n* = 1.5
0.1	−2.54E-02	−6.34E-02	−6.69E-02
0.2	−4.73E-02	−1.14E-01	−1.13E-01
0.3	−7.59E-02	−1.63E-01	−1.56E-01
0.4	−1.12E-01	−2.02E-01	−2.01E-01
0.5	−1.39E-01	−2.14E-01	−2.32E-01
0.6	−1.34E-01	−1.81E-01	−2.26E-01
0.7	−9.53E-02	−9.82E-02	−1.43E-01
0.8	−3.22E-02	4.72E-02	7.80E-02
0.9	1.25E-01	3.58E-01	4.59E-01

4.2. *Re* = 400

The consistency index μ_0 was next set to be 0.0025 to obtain the desired Reynolds number of 400 with the same fluid density, top wall shear velocity and domain length as the previous Reynolds number. For the Newtonian fluid case ($n = 1$) the fluid dynamic viscosity was a constant and equals the consistency index 0.0025. Figure 9 shows streamlines and contours of viscosity for the shear-thinning case ($n = 0.5$) at different z planes. In these figures, similar to $Re = 100$ we observe only one large eddy centred in the region close the right side of the top moving wall. As expected, high viscosity regions are observed close to the bottom front and back edges due to the slow motion of the fluid. It can be seen that in most region of the cavity the viscosity is in the range of 0.002–0.02. The lowest viscosity region is seen at the top downstream edge of the cavity which is similar to observation at $Re = 100$. Also, locally high shear regions are found in the region close to $(x, y) \approx (0.2, 0.8)$ in planes away from the side walls. That local high viscosity regions have a viscosity about five times the consistency index ($\mu_0 = 0.0025$) which is again similar to what we see at $Re = 100$. The flow patterns at $Re = 400$ are similar qualitatively but differ in the magnitudes of local viscosity and velocities.

Figure 10 plots contours of viscosity and streamlines at different z planes for the shear-thickening fluid. The corresponding viscosity contours indicate that for a shear-thickening fluid the effective viscosity is below 0.004

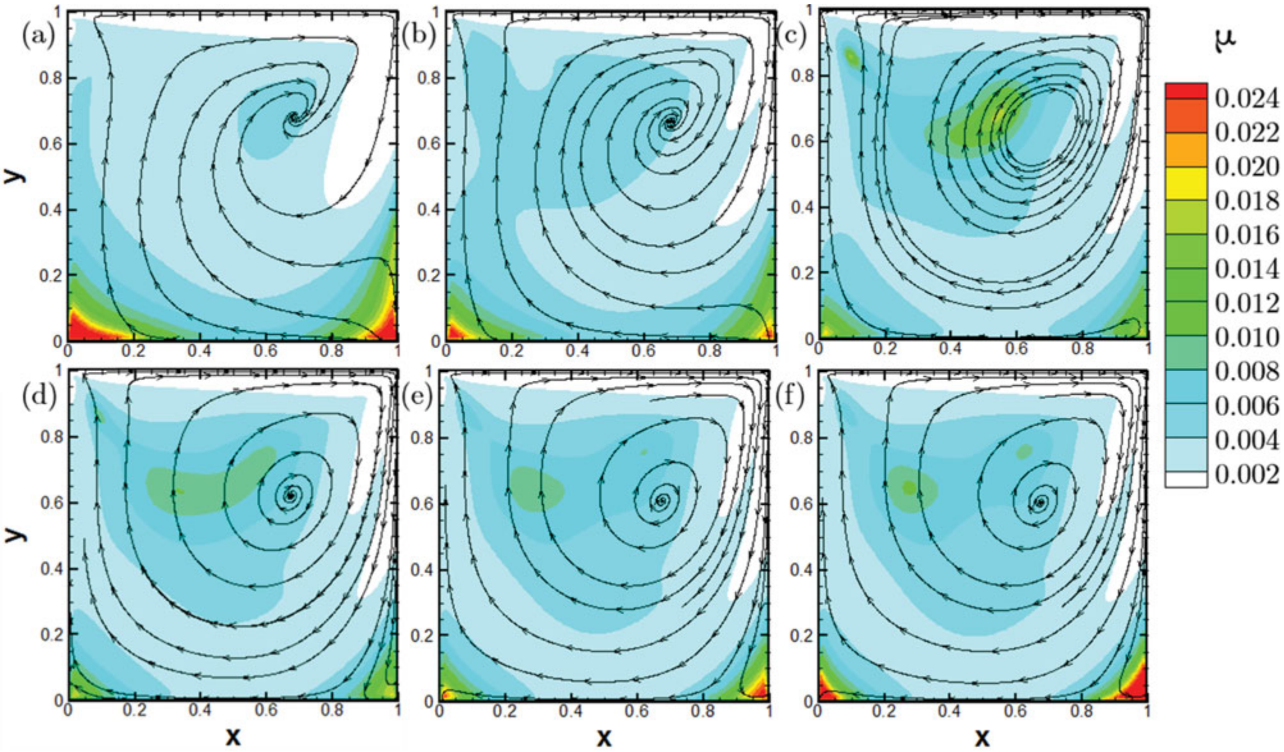

Figure 9. Contours of viscosity and streamlines at different z planes: (a) $z = 0.05$; (b) $z = 0.1$; (c) $z = 0.2$; (d) $z = 0.3$; (e) $z = 0.4$; (f) $z = 0.5$ for $Re = 400$ and $n = 0.5$.

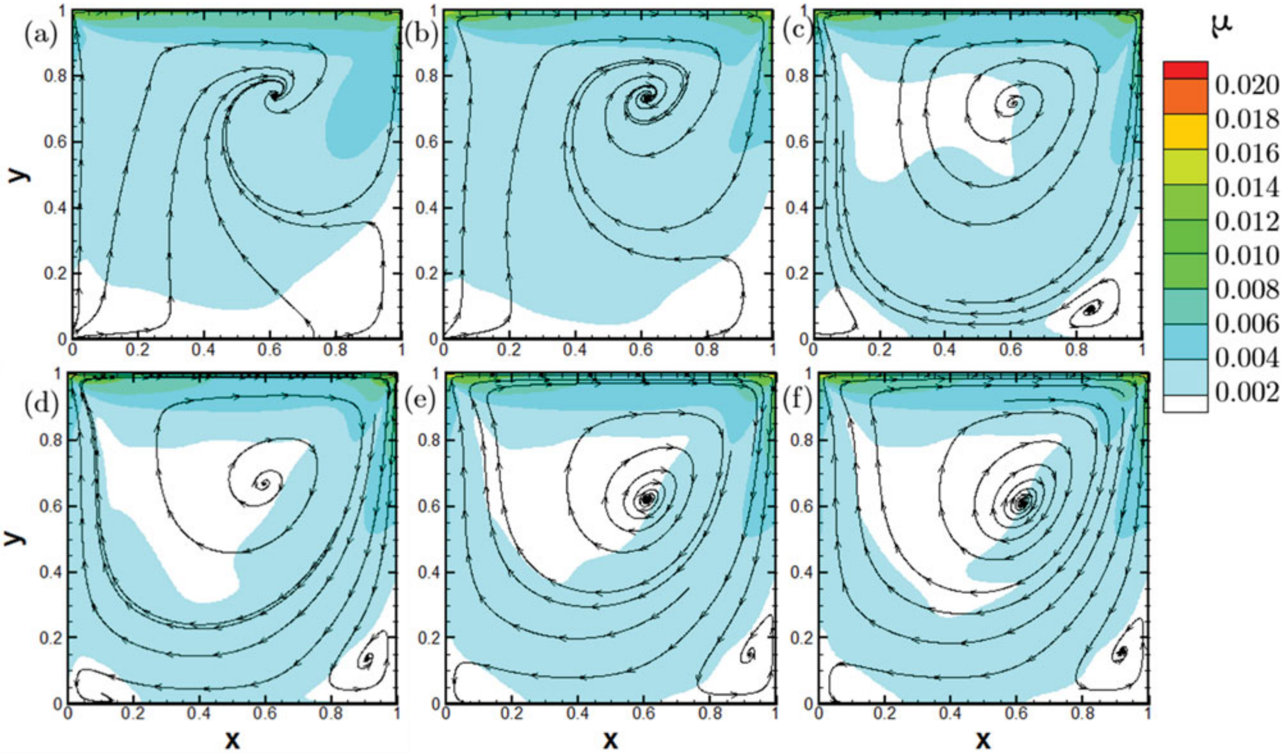

Figure 10. Contours of viscosity and streamlines at different z planes: (a) $z = 0.05$; (b) $z = 0.1$; (c) $z = 0.2$; (d) $z = 0.3$; (e) $z = 0.4$; (f) $z = 0.5$ for $Re = 400$ and $n = 1.5$.

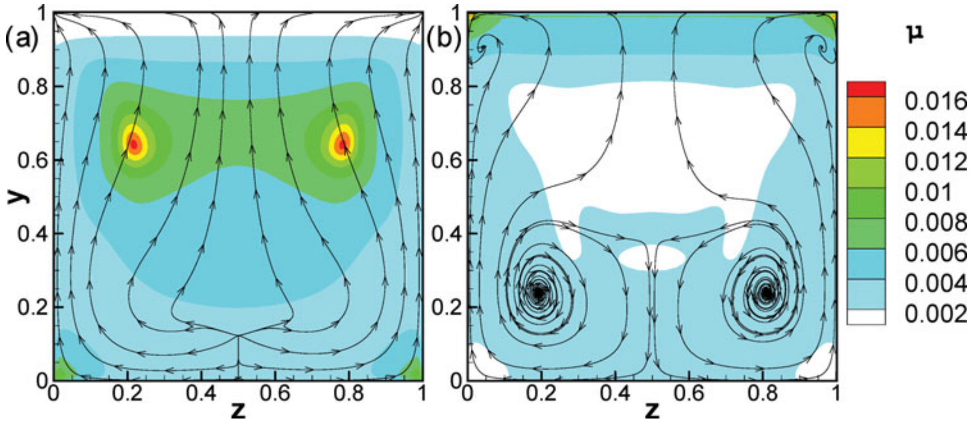

Figure 11. Contour plots of viscosity and streamlines in plane $x = 0.5$ for $n = 0.5$ (left) and $n = 1.5$ (right), $Re = 400$.

(around two times the consistency index) in most regions of the cavity. Still as expected, very high viscosity regions were found at the top front and back edges due to the high shear and two very small eddies are formed at the two bottom corners (low viscosity region) far from the side walls. It is also seen that local low viscosity ($\mu < 0.002$) regions are found close to all the eddy centres, and the effective viscosity of region in the bottom half ($y < 0.5$) of the cavity is close to the consistency index $\mu_0 = 0.0025$.

Figure 11(a) and (b) show the contour plots of viscosity and streamlines in the plane $x = 0.5$ for $n = 0.5$ and n = 1.5, respectively. For the shear-thinning fluid, the results show that the low viscosity regions are close to the top moving wall ($y = 1$). There are two local high viscosity regions ($\mu > 6\mu_0$) at two spots symmetrical to the z plane, $(z, y) = (0.2, 0.64)$ and $(0.8, 0.65)$. The streamlines on the middle x plane for the shear-thickening fluid are ($n = 1.5$) shown in Figure 11(b). For a shear-thickening fluid, we see four vortices close to the two side planes. The viscosity contour plot again shows that low viscosity region is in the bottom part of the cavity and high viscosity region is close to the top moving wall, but it is noticeable that as one moves down from the top wall, a low viscosity region is seen at the centre region of the cavity.

The relative viscosity μ/μ_0 on horizontal and vertical centrelines of the symmetry plane is again plotted in Figure 12(a) and (b), respectively, for $Re = 400$. On the horizontal centreline, the viscosity variation for shear thickening fluid $n = 1.5$ ranges from 0.6 to 1.7. Moving from left wall towards the right wall, the relative viscosity ratio first drops from 1.55 to 0.6 and then slightly varies until it reaches $x = 0.8$. After that it increases to a maximum of 1.7 at $x = 0.9$ which is close to the right wall. For the shear-thinning fluid ($n = 0.5$) the maximum high relative viscosity region ($\mu/\mu_0 = 2.6$) is seen close to the upstream side wall at $x = 0.3$. It then drops as we move towards the right wall to reach a minimum at $x = 0.97$. Subsequently it increases to around 0.9 in a region very close to the wall. A very sudden drop of the relative viscosity was seen at region $0.7 < x < 0.8$ which corresponds to the right side of the main eddy where the flow is mainly moving downward. The relative viscosity on the vertical centreline for case

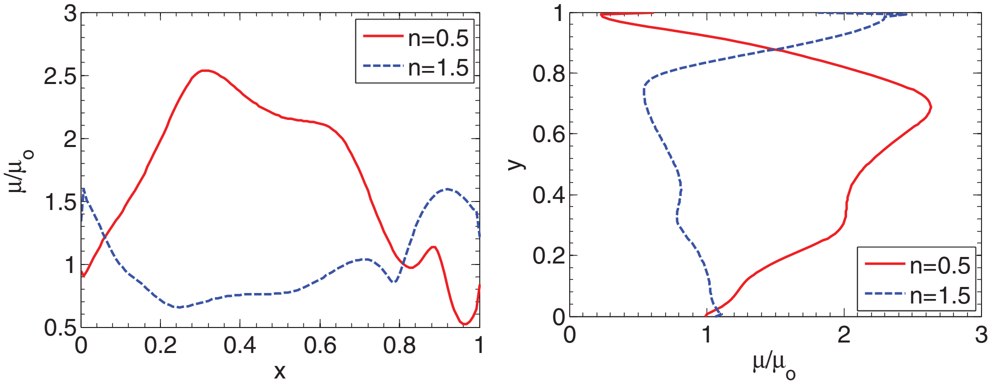

Figure 12. Relative viscosity on horizontal (left) and vertical (right) centrelines for $n = 0.5$ and $n = 1.5$, $Re = 400$.

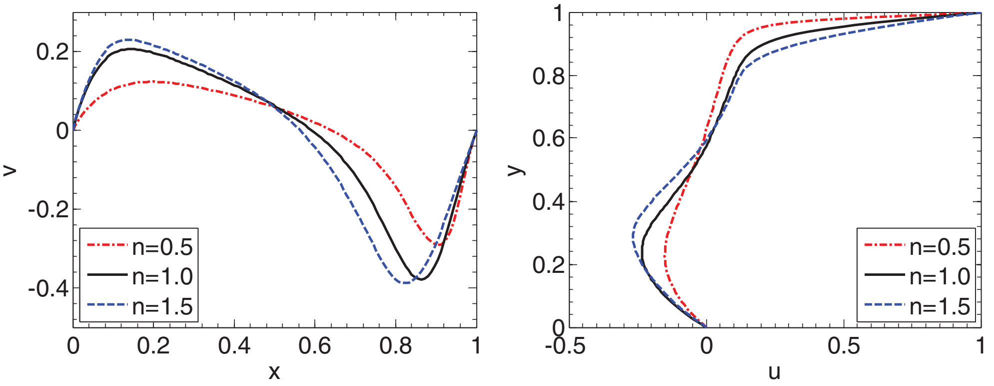

Figure 13. *v*-velocity on horizontal centreline (left) and *u* velocity on vertical centreline (right) for $Re = 400$.

Table 2. *v* velocity on horizontal centreline and *u* velocity on vertical centreline at $Re = 400$.

v velocity on horizontal centreline			
x	$n = 0.5$	$n = 1.0$	$n = 1.5$
0.1	1.04E-01	1.95E-01	2.19E-01
0.2	1.23E-01	1.97E-01	2.16E-01
0.3	1.11E-01	1.60E-01	1.75E-01
0.4	8.82E-02	1.15E-01	1.25E-01
0.5	5.87E-02	6.20E-02	5.83E-02
0.6	1.98E-02	−6.25E-03	−4.30E-02
0.7	−3.62E-02	−1.14E-01	−2.02E-01
0.8	−1.44E-01	−3.01E-01	−3.79E-01
0.9	−2.89E-01	−3.37E-01	−2.87E-01
v velocity on horizontal centreline			
y	$n = 0.5$	$n = 1.0$	$n = 1.5$
0.1	−1.03E-01	−1.50E-01	−1.41E-01
0.2	−1.49E-01	−2.27E-01	−2.33E-01
0.3	−1.39E-01	−2.17E-01	−2.65E-01
0.4	−9.80E-02	−1.37E-01	−1.99E-01
0.5	−5.02E-02	−5.05E-02	−8.95E-02
0.6	−8.91E-03	1.34E-02	4.26E-03
0.7	2.56E-02	6.07E-02	7.06E-02
0.8	5.94E-02	1.06E-01	1.25E-01
0.9	1.07E-01	2.14E-01	3.42E-01

$n = 0.5$ shows that as we traverse downward from the top wall ($y = 1.0$) the relative viscosity first increases from 0.2 to 2.5, and reaches the maximum value at $y = 0.75$. For $n = 1.5$, as we move from $y = 1.0$ to $y = 0.75$, the relative viscosity decreases from 2.5 to 0.6, then increases to 1.1 at the bottom wall region.

The v velocity profile on horizontal centre line and u velocity profile on vertical centreline for the two different fluids for $Re = 400$ are plotted in Figure 13(a) and (b), respectively. The v velocity profile on the horizontal centreline shows that the peak velocity increases as n increases, and the maximum peak v velocity for the shear-thickening fluid is closer to the upstream wall ($x = 0$) and is twice that with $n = 0.5$. The lines clearly show that for the shear-thinning fluid the downstream side peak velocity is much closer to the wall at $x = 1$. Comparing the location of this negative peak velocity we see that the boundary layer is slightly thinner for the shear-thinning fluid ($n = 0.5$). This effect is not easily seen from the case at $Re = 100$. For the u velocity on the vertical centreline, the results also show that the magnitude of the peak negative u velocity for $n = 1.5$ is slightly higher than that of the Newtonian fluid but twice the value for shear-thinning fluid with $n = 0.5$. The peak negative u velocity happens at higher y for the shear-thickening fluid. Selected points of Figure 13 were tabulated in Table 2.

4.3. *Re = 1000*

We next consider an even higher Reynolds number of 1000. For this case, μ_0 was set to be 0.001. As before three cases are considered with $n = 0.5$, 1.0 and 1.5. The results for $n = 1.0$ matched quite closely with previous published Newtonian fluid results. Here we present results for $n = 0.5$ and 1.5 and contrast them with results presented earlier at $Re = 100$ and 400.

Figure 14 presents streamlines and contours of viscosity at different constant z planes for the shear-thinning fluid. For $Re = 1000$ we again observe that close to the side walls only one big eddy exists, but as we move towards the centre a smaller eddy is formed in the right bottom corner. Because of the shear thinning property, the viscosity is computed to be larger than μ_0. As a result, these corner vortices are relatively weaker than those observed for a Newtonian fluid. We also see that there are a few regions inside the main interior domain where the computed viscosity is again high. These regions have low shear and therefore high viscosity. Figure 14(d), (e) and (f) show that as the position of the plane moves away from the left side wall, a local high viscosity region is developed in region enclosed in the dashed square. We observe that at the symmetry plane ($z = 0.5$) the local maximum viscosity in the region surrounded by the dashed square can be

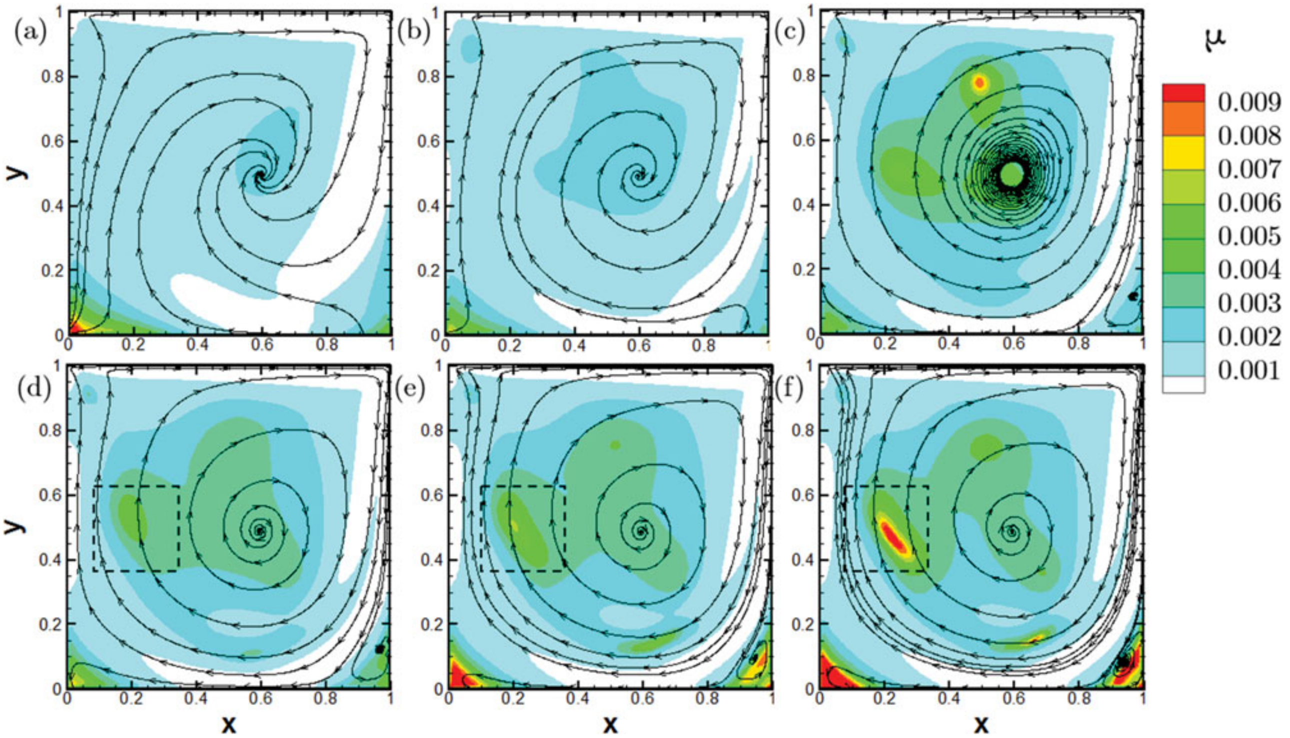

Figure 14. Contours of viscosity and streamlines at different *z* planes: (a) $z = 0.05$; (b) $z = 0.1$; (c) $z = 0.2$; (d) $z = 0.3$; (e) $z = 0.4$; (f) $z = 0.5$ for $Re = 1000$ and $n = 0.5$.

as much as 10 times the consistency index. This is again a region of low shear but large velocities.

Figure 15 plots contour of viscosity and streamlines at different *z* planes for the shear-thickening case. The corresponding viscosity contours indicate that for a shear-thickening fluid the effective viscosity is below 0.002 which is two times the consistency index. A very high viscosity region (not seen clearly) was found at the top front and back edges due to the high shear. The streamlines show that in contrast to the shear-thinning case, two small eddies are formed at the two bottom corners at the planes far enough ($z = 0.2$) from the side walls. This is similar to the observation for a Newtonian fluid. It is also seen that local low viscosity ($\mu < 0.001$) regions are found close to the all the eddy centres.

Figure 16 shows the contour plots of viscosity and streamlines in plane at $x = 0.5$ for $n = 0.5$ and $n = 1.5$, respectively. For $n = 0.5$, the results show that there are two high viscosity regions, $(z, y) \approx (0.2, 0.8)$ and $(z, y) \approx (0.8, 0.8)$, close to the top moving wall ($y = 1$). Compared with the case of $Re = 400$, these two spots move upward from $z = 0.7$ to $z = 0.8$. In the middle *x* plane, the computations show swirling flow at the top corners close to the top wall, which were not seen for case with $Re = 100$ or 400. The streamlines on the middle *x* plane for the shear-thickening fluid ($n = 1.5$) are also shown in Figure 16. For a shear-thickening fluid, we see four vortices close to the two side planes. The viscosity contours indicate that the low viscosity region is relatively in the middle part of the cavity and high viscosity region is close to the top moving wall. It also shows that slightly high viscosity region at the bottom of the cavity, in the boundary layer.

The relative viscosity μ/μ_0 on horizontal and vertical centrelines of the symmetry plane is plotted in Figure 17(a) and (b), respectively, for the variable viscosity cases. On the horizontal centreline, the viscosity variation for shear thickening fluid $n = 1.5$ is not very large. However, for the shear thinning fluid the maximum relative viscosity can be more than nine times larger than the consistency index μ_0, and the minimum relative viscosity can be 0.4. This indicates that ratio of local maximum viscosity to the minimum viscosity along the horizontal centre line for $n = 0.5$ can be as large as 36. The location of the high viscosity region was seen at $x = 0.2$ which agreed with the contour plot of viscosity in Figure 18(a). The relative viscosity on the vertical centreline for case $n = 0.5$ shows that as we traverse downward from the top wall ($y = 1.0$) to the bottom wall, the relative viscosity first increases from 0.02 to 4.4, reaches a maximum value at $y = 0.75$ and then it decreases to 2 at $y = 0.2$. It increases again to 2.8 at $y = 0.15$, eventually decreasing at the bottom because of larger shear again. For $n = 1.5$, as we move from $y = 1.0$ to $y = 0.7$, the relative viscosity decreases from 3 to 0.4, but again slowly increases and

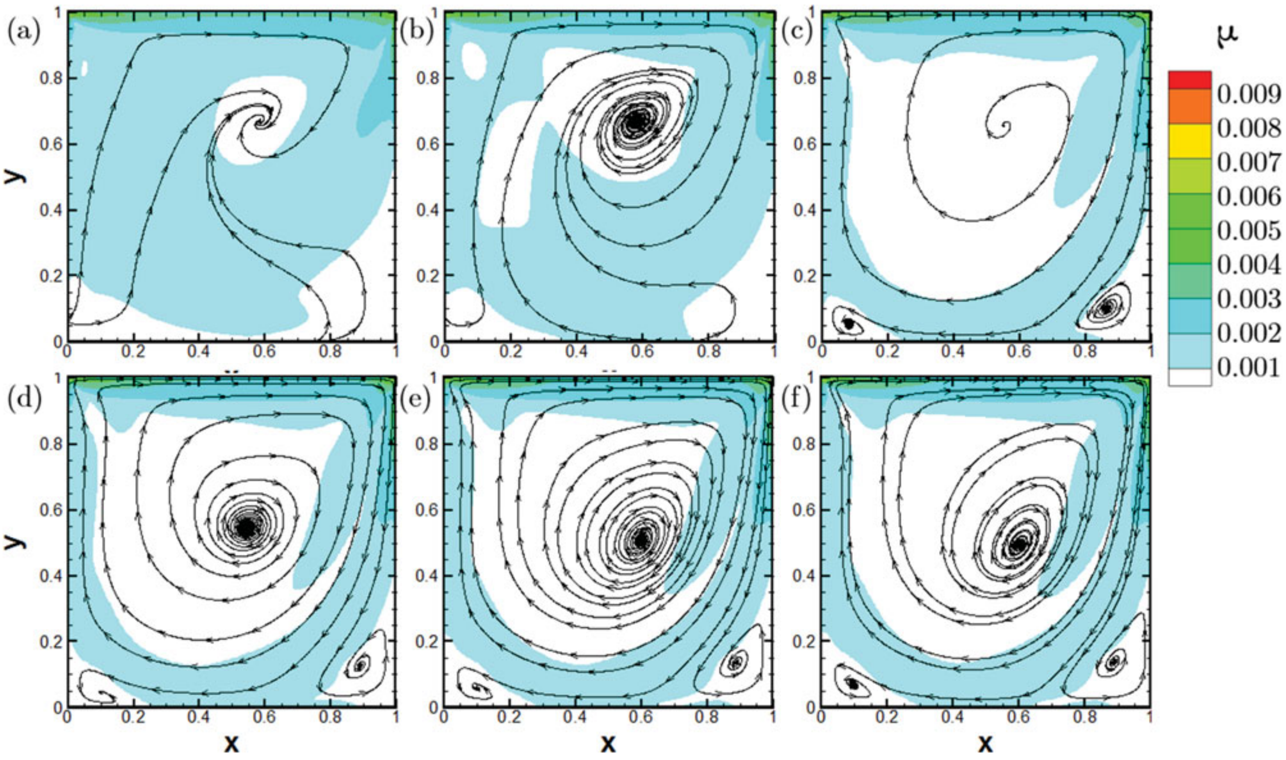

Figure 15. Contours of viscosity and streamlines at different z planes: (a) $z = 0.05$; (b) $z = 0.1$; (c) $z = 0.2$; (d) $z = 0.3$; (e) $z = 0.4$; (f) $z = 0.5$ for $Re = 1000$ and $n = 1.5$.

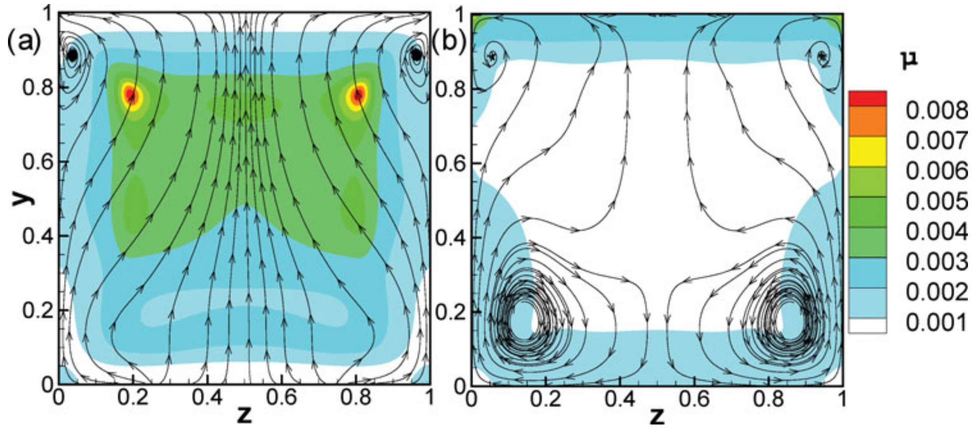

Figure 16. Contour plots of viscosity and streamlines in plane $x = 0.5$ for $n = 0.5$ (left) and $n = 1.5$ (right), $Re = 1000$.

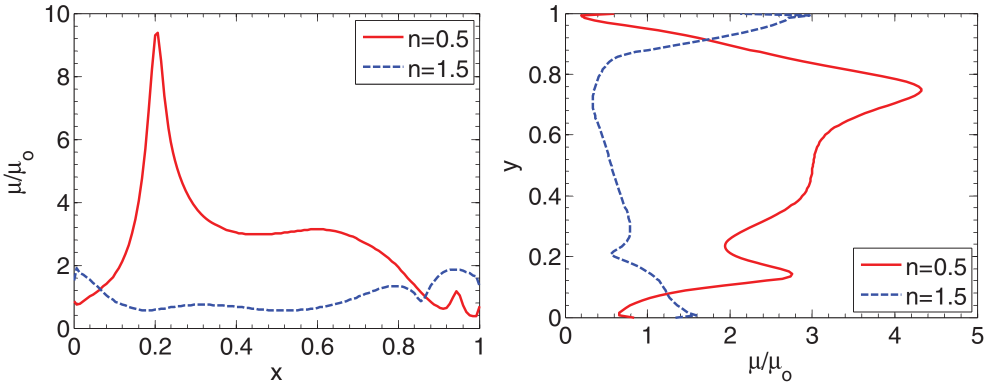

Figure 17. Relative viscosity on horizontal (left) and vertical (right) centreline for $n = 0.5$ and $n = 1.5$, $Re = 1000$.

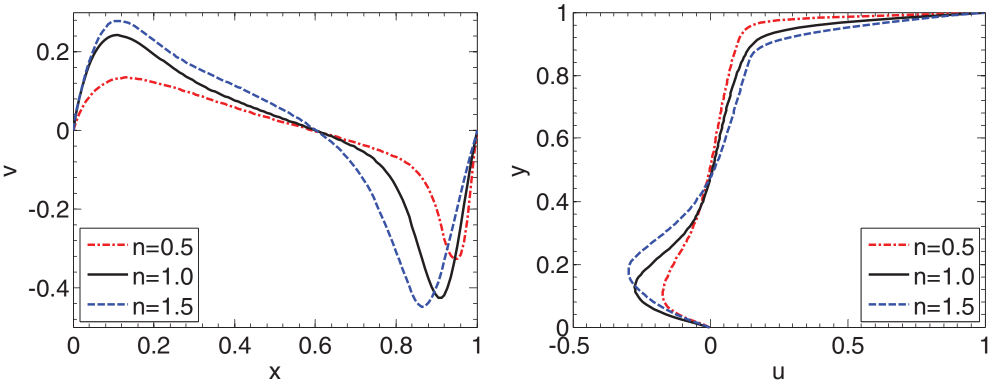

Figure 18. *v* velocity on horizontal centreline (left) and *u* velocity on vertical centreline (right) for $Re = 1000$.

Table 3. *v* velocity on horizontal centreline and *u* velocity on vertical centreline.

v velocity on horizontal centreline

x	$n = 0.5$	$n = 1.0$	$n = 1.5$
0.1	1.29E-01	2.40E-01	2.76E-01
0.2	1.23E-01	1.94E-01	2.29E-01
0.3	9.26E-02	1.25E-01	1.63E-01
0.4	5.84E-02	7.64E-02	1.14E-01
0.5	2.72E-02	3.74E-02	6.40E-02
0.6	−1.55E-03	3.75E-04	1.32E-03
0.7	−3.13E-02	−4.32E-02	−9.57E-02
0.8	−6.82E-02	−1.43E-01	−3.09E-01
0.9	−2.02E-01	−4.19E-01	−3.96E-01

u velocity on vertical centreline

y	$n = 0.5$	$n = 1.0$	$n = 1.5$
0.1	−1.72E-01	−2.65E-01	−2.35E-01
0.2	−1.34E-01	−2.15E-01	−2.93E-01
0.3	−7.11E-02	−9.23E-02	−1.66E-01
0.4	−2.97E-02	−2.67E-02	−5.24E-02
0.5	−1.59E-03	7.64E-03	1.36E-02
0.6	2.07E-02	3.39E-02	5.58E-02
0.7	4.23E-02	6.14E-02	9.13E-02
0.8	6.68E-02	9.58E-02	1.25E-01
0.9	9.86E-02	1.56E-01	2.11E-01

Table 4. Vortex center location (*x*, *y*) on symmetry plane.

n	$Re = 100$	$Re = 400$	$Re = 1000$
$n = 0.5$	(0.716, 0.815)	(0.674, 0.605)	(0.593, 0.485)
$n = 1.0$	(0.619, 0.762)	(0.623, 0.575)	(0.594, 0.465)
$n = 1.5$	(0.579, 0.763)	(0.616, 0.610)	(0.600, 0.496)

then decreases to another local minimum value of 0.5 at $y = 0.2$. After that, moving down the cavity, the viscosity increases again.

The velocities on horizontal and vertical centrelines for the three different fluids are plotted in Figure 18. The v velocity on horizontal centreline shows that the peak velocity increases as n increases, and the maximum peak v velocity for the shear-thickening fluid ($n = 1.5$) is closer to the upstream wall ($x = 0$) can be twice that with $n = 0.5$. These plots also show that for shear thinning fluid ($n = 0.5$) the peak velocity is closer to the side wall. For the u velocity on the vertical centreline, the results also show that the peak u velocity for $n = 1.5$ is slighter higher than that of the Newtonian fluid but twice the value for shear-thinning fluid with $n = 0.5$. The boundary layer for the shear-thinning fluid is thinner at bottom wall. Selected points on the six lines in Figure 18 were tabulated in Table 3. These trends are same as observed for $Re = 100$ and $Re = 400$, but the values are different.

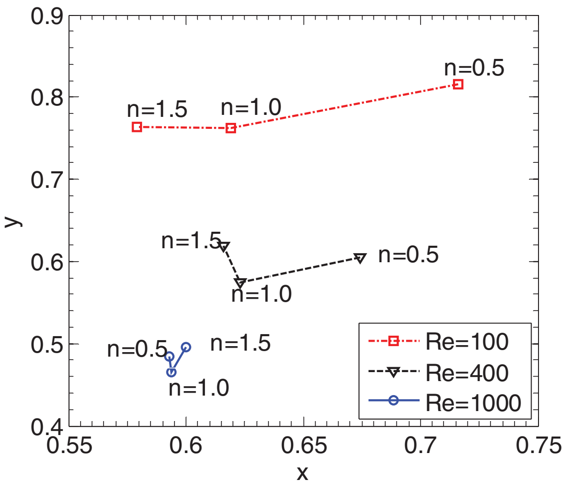

Figure 19. Vortex centre on the symmetry plane for all nine cases.

4.4. *Centres of the main vortices*

It is interesting to monitor the movement of the main vortex in the centre of the cavity as a function of the power law index and the flow Reynolds number. Table 4 shows all the centres of the main vortices in the symmetry plane and Figure 19 shows the centres graphically. For $Re = 100$ and 400, as n increases from 0.5 to 1.5 the centre of the vortex moves from right wall towards the centre, while it first moves down and then moves up. However, for $Re = 1000$, as n increases from 0.5 to 1.5 the x coordinate of the centre moves from a place close to the centre towards the right wall. In all of these cases, for fixed Re the lowest centre location can be reached when $n = 1.0$. The results also show that the non-Newtonian effect on the location of the centre of the vortex is more important when the Reynolds number is low. As the Reynolds number increases, the effect of n on centre location of the vortex is significantly attenuated.

5. Conclusion

The 3D flow of a power-law fluid in a driven cube at $Re = 100$, 400 and 1000 for three values of the power law index have been studied. The three Reynolds numbers are seen to give the expected behaviour of shear-thinning and shear-thickening fluids. The flow patterns, velocity profiles and viscosity distributions are as per expectations, and show similar behaviour at the three Reynolds numbers. The 3D behaviour is reflected in Taylor-Goertler like vortices in the corners along the spanwise direction. Tables of the velocity distribution along the centrelines are given for benchmarking of other studies. The key observations of this study are the distributions of the viscosity, the effects of the non-Newtonian behaviour on the velocity profiles and the streamlines. In all the cases studied, steady flow was obtained.

Nomenclature

U	moving wall speed, m/s
$\underline{\underline{\tau}}$	deviatoric part of the Cauchy stress tensor
ρ	density of the fluid, kg/m^3
p	pressure of the fluid, pa
$\vec{u}$	velocity vector of the fluid and $\vec{u} = (u_1, u_2, u_3)$, m/s
$\underline{\underline{\varepsilon}}$	strain rate tensor
μ	effective dynamic viscosity, kg/(m·s)
μ_0	consistency index in power-law model
n	flow behaviour index of the non-Newtonian fluid
Re	Reynolds number
L	the dimension of the cavity, m

Acknowledgements

The authors thank the financial supports from the National Science Foundation (Grant No. CMMI 11-30882) and the Continuous Casting Consortium, University of Illinois at Urbana-Champaign, USA. This research is also part of the Blue Waters sustained-petascale computing project, which is supported by the National Science Foundation (awards OCI-0725070 and ACI-1238993) and the state of Illinois. Blue Waters is a joint effort of the University of Illinois at Urbana-Champaign and its National Center for Supercomputing Applications. The authors would like to thank Prof. R. Ewoldt for initial comments on the manuscript. We also thank NVIDIA Hardware Grant Program for providing the GPUs.

Disclosure statement

No potential conflict of interest was reported by the authors.

Funding

National Science Foundation [Grant Number CMMI 11-30882]; the Continuous Casting Consortium, University of Illinois at Urbana-Champaign, USA; National Science Foundation [Awards OCI-0725070 and ACI-1238993].

References

Albensoeder, S., and H. C. Kuhlmann. 2005. “Accurate Three-Dimensional Lid-Driven Cavity Flow.” *Journal of Computational Physics* 206 (2): 536–558.

Albensoeder, S., H. C. Kuhlmann, and H. J. Rath. 2001. “Three-Dimensional Centrifugal-Flow Instabilities in the Lid-Driven-Cavity Problem.” *Physics of Fluids* 13 (1): 121–135.

Arnal, M., O. Lauer, Ž. Lilek, and M. Perić. 1992. “Prediction of Three-Dimensional Unsteady Lid-Driven Cavity Flow.” In *Numerical Simulation of 3-D Incompressible Unsteady Viscous Laminar Flows*, edited by M. Deville, T.-H. Le, and Y. Morchoisne, 13–24. Vieweg+Teubner Verlag.

Aydin, M., and R. T. Fenner. 2001. “Boundary Element Analysis of Driven Cavity Flow for Low and Moderate Reynolds Numbers.” *International Journal for Numerical Methods in Fluids* 37 (1): 45–64.

Backx, E., and H. J. Wirz. 1975. “Numerical Solution of the Navier-Stokes Equations for a 3-D Driven Cavity Flow.” GAMM Conference on Numerical Methods in Fluid Mechanics, DVFLR, Cologne, October 8–10.

Bell, B. C., and K. S. Surana. 1994. “p-Version Least Squares Finite Element Formulation for Two-Dimensional, Incompressible, Non-newtonian Isothermal and Non-isothermal Fluid Flow.” *International Journal for Numerical Methods in Fluids* 18 (2): 127–162.

Bhatnagar, P. L., E. P. Gross, and M. Krook. 1954. “A Model for Collision Processes in Gases. I. Small Amplitude Processes in Charged and Neutral One-Component Systems.” *Physical Review* 94 (3): 511.

Bruneau, C. H., and M. Saad. 2006. “The 2D Lid-Driven Cavity Problem Revisited.” *Computers and Fluids* 35 (3): 326–348.

Bustamante, C. A., W. F. Florez, H. Power, M. Giraldo, and A. F. Hill. 2011. “Control Volume-Radial Basis Function Solution of 2D Driven Cavity Flow in Terms of the Velocity-Vorticity Formulation.” *Computer Modeling in Engineering and Sciences* 79 (2): 103–130.

Cantaloube, B., and T. H. Le. 1992. “Direct Simulation of Unsteady Flow in a Three-Dimensional Lid-Driven Cavity.” In *Numerical Simulation of 3-D Incompressible Unsteady Viscous Laminar Flows*, edited by M. Deville, T. -H. Le, and Y. Morchoisne, 25–33. Vieweg+Teubner Verlag.

Chaudhary, R. 2011. “Studies of Turbulent Flows in Continuous Casting of Steel with and without Magnetic Field.” Ph.D. thesis., University of Illinois at Urbana-Champaign, IL.

Cortes, A. B., and J. D. Miller. 1994. “Numerical Experiments with the Lid Driven Cavity Flow Problem.” *Computers and Fluids* 23 (8): 1005–1027.

Darr, J. H., and S. P. Vanka. 1991. “Separated Flow in a Trapezoidal Cavity.” *Physics of Fluids A* 3: 385.

De Vicente, J., D. Rodríguez, V. Theofilis, and E. Valero. 2011. “Stability Analysis in Spanwise-Periodic Double-Sided Lid-Driven Cavity Flows with Complex Cross-Sectional Profiles.” *Computers & Fluids* 43 (1): 143–153.

De, S., K. Nagendra, and K. N. Lakshmisha. 2009. “Simulation of Laminar Flow in a Three-Dimensional Lid-Driven Cavity by Lattice Boltzmann Method.” *International Journal of Numerical Methods for Heat and Fluid Flow* 19 (6): 790–815.

Deshpande, M. D., and S. G. Milton. 1998. “Kolmogorov Scales in a Driven Cavity Flow.” *Fluid Dynamics Research* 22 (6): 359–381.

Deshpande, M. D., and P. N. Shankar. 1993. “Structure of Laminar Flow in a Three-Dimensional Driven Cavity.” *Proceedings of the Fluid Dynamics Symposium in Honour of Professor R. Narasimha on his 60th Birthday, 9 Jul 1993*, Sikkim.

Dong, D. B., S. J. Shi, Z. X. Hou, and W. S. Chen. 2014. “Numerical Simulation of Viscous Flow in a 3D Lid-Driven Cavity Using Lattice Boltzmann Method.” *Applied Mechanics and Materials* 444: 395–399.

Elias, R. N., M. A. Martins, and A. L. Coutinho. 2006. “Parallel Edge-Based Solution of Viscoplastic Flows with the SUPG/PSPG Formulation.” *Computational Mechanics* 38 (4-5): 365–381.

Freitas, C. J., R. L. Street, A. N. Findikakis, and J. R. Koseff. 1985. “Numerical Simulation of Three-Dimensional Flow in a Cavity.” *International Journal for Numerical Methods in Fluids* 5 (6): 561–575.

Gao, W., and R. Liu. 2009 “A Hybrid Finite Volume/Finite Element Method for Incompressible Generalized Newtonian Fluid Flows on Unstructured Triangular Meshes.” *Acta Mechanica Sinica* 25 (6): 747–760.

Ghia, U., K. N. Ghia, and C. T. Shin. 1982. “High-Re Solutions for Incompressible Flow Using the Navier-Stokes Equations and a Multigrid Method.” *Journal of Computational Physics* 48 (3): 387–411.

Glowinski, R., G. Guidoboni, and T.-W. Pan. 2006. “Wall-Driven Incompressible Viscous Flow in a Two-Dimensional Semi-Circular Cavity.” *Journal of Computational Physics* 216 (1): 76–91.

González, L. M., M. Ahmed, J. Kühnen, H. C. Kuhlmann, and V. Theofilis. 2011. “Three-Dimensional Flow Instability in a Lid-Driven Isosceles Triangular Cavity.” *Journal of Fluid Mechanics* 675: 369–396.

Grillet, A. M., B. Yang, B. Khomami, and E. S. G. Shaqfeh. 1999. “Modeling of Viscoelastic Lid Driven Cavity Flow using Finite Element Simulations.” *Journal of Non-Newtonian Fluid Mechanics* 88 (1–2): 99–113.

Guermond, J. L., C. Migeon, G. Pineau, and L. Quartapelle. 2002. “Start-Up Flows in a Three-Dimensional Rectangular Driven Cavity of Aspect Ratio 1:1:2 at Re = 1000.” *Journal of Fluid Mechanics* 450: 169–199.

Guo, X., C. Zhong, C. Zhuo, and J. Cao. 2014. “Multiple-Relaxation-Time Lattice Boltzmann Method for Study of Two-Lid-Driven Cavity Flow Solution Multiplicity.” *Theoretical and Computational Fluid Dynamics* 28 (2): 215–231.

Gupta, M. M., R. P. Manohar, and J. W. Stephenson. 1983. “A High Order Finite Difference Method for Fluid Flow Problems.” In *Proceedings of the Tenth World Congress on System Simulation and Scientific Computation*, Vol. 1 (A84-11828 02-59), 212–214, 1982 August 8–13, Montreal, Canada. Montreal: International Association for Mathematics and Computers in Simulation.

Haque, S., I. Lashgari, F. Giannetti, and L. Brandt. 2012. “Stability of Fluids with Shear-Dependent Viscosity in the Lid-Driven Cavity.” *Journal of Non-Newtonian Fluid Mechanics* 173: 49–61.

Heaton, C. J. 2008. “On the Appearance of Moffatt Eddies in Viscous Cavity Flow as the Aspect Ratio Varies.” *Physics of Fluids* 20 (10): 103102 (11 pp).

Huang, Y., U. Ghia, G. A. Osswald, and K. N. Ghia. 1992. “Velocity-Vorticity Simulation of Unsteady 3-D Viscous Flow within a Driven Cavity.” In *Numerical Simulation of 3-D Incompressible Unsteady Viscous Laminar Flows*, edited by M. Deville, T.-H. Le, and Y. Morchoisne, 54–66. Vieweg+Teubner Verlag.

Huser, A., and S. Biringen. 1992. “Calculation of Two-Dimensional Shear-Driven Cavity Flows at High Reynolds Numbers.” *International Journal for Numerical Methods in Fluids* 14 (9): 1087–1109.

Iwatsu, R., K. Ishii, T. Kawamura, K. Kuwahara, and J. M. Hyun. 1989. “Numerical Simulation of Three-Dimensional Flow Structure in a Driven Cavity.” *Fluid Dynamics Research* 5 (3): 173.

Jordan, S. A., and S. A. Ragab. 1994. “On the Unsteady and Turbulent Characteristics of the Three-Dimensional Shear-Driven Cavity Flow.” *ASME Journal of Fluids Engineering* 116 (3): 439–449.

Jyotsna, R. and S. P. Vanka. 1995. “Multigrid Calculation of Steady, Viscous Flow in a Triangular Cavity.” *Journal of Computational Physics* 122 (1): 107–117.

Jyotsna, R., and S. P. Vanka. 1996. “A Pressure Based Multigrid Procedure for the Navier–Stokes Equations on Unstructured Grids.” In *Seventh Copper Mountain Conference on Multigrid Methods NASA Conference Publication 3339*, edited by N. D. Melson, T. A. Manteuffel, S. F.Mc. Cormick, and C. C. Douglas, 409–424. Hampton, VA: NASA.

Kalita, J. C., and M. M. Gupta. 2010. “A Streamfunction-Velocity Approach for 2D Transient Incompressible Viscous Flows.” *International Journal for Numerical Methods in Fluids* 62 (3): 237–266.

Kirk, D. B., and W. W. Hwu. 2012. *Programming Massively Parallel Processors – A Hands-on Approach*. 2nd ed. Morgan Kaufmann.

Kondo, N., N. Tosaka, and T. Nishimura. 1991. “Third-Order Upwind Finite Element Formulations for Incompressible Viscous Flow Problems.” *Computer Methods in Applied Mechanics and Engineering* 93 (2): 169–187.

Koseff, J. R., and R. L. Street. 1984. “The Lid-Driven Cavity Flow: A Synthesis of Qualitative and Quantitative Observations.” *ASME Journal of Fluids Engineering* 106 (4): 390–398.

Ku, H. S., R. S. Hirsh, and T. D. Taylor. 1987 “A Psuedo-Spectral Method for Solution of the Three-Dimensional

Incompressible Navier-Stokes Equations." *Journal of Computational Physics* 70: 439.

Leonard, B. P. 1981. "A Survey of Finite Differences with Upwinding for Numerical Modelling of the Incompressible Convective Diffusion Equation." *Computational Techniques in Transient and Turbulent Flow* 2: 1–35.

Leriche, E., S. Gavrilakis, and G. Labrosse. 2000. "Direct Numerical Simulation of Lid-Driven Cavity Flow within a 3D Inhomogeneous Domain on an NEC-SX4 Supercomputer." *International Conference on Applications of High-Performance Computing in Engineering*. doi:10.2495/HPC000331

Li, Q., N. Hong, B. Shi, and Z. Chai. 2014. "Simulation of Power-Law Fluid Flows in Two-Dimensional Square Cavity using Multi-Relaxation-Time Lattice Boltzmann Method." *Communications in Computational Physics* 15 (1): 265–284

Mendu, S. S., and P. K. Das. 2012. "Flow of Power-Law Fluids in a Cavity Driven by the Motion of Two Facing Lids: A Simulation by Lattice Boltzmann Method." *Journal of Non-Newtonian Fluid Mechanics* 175: 10–24.

Mitsoulis, E., and T. Zisis. 2011. "Flow of Bingham Plastics in a Lid-Driven Square Cavity". *Journal of Non-Newtonian Fluid Mechanics* 101 (1): 173–180.

Neofytou, P. 2005. "A Third-Order Upwind Finite Volume Method for Generalised Newtonian Fluid Flows." *Advances in Engineering Software* 36 (10): 664–680.

NVIDIA. 2011. *NVidia CUDA C Programming Guide, Version 4.0*. Santa Clara, CA: NVIDIA. https://docs.nvidia.com/cuda/cuda-c-programming-guide/

Papanastasiou, T. C. 1987. "Flows of Materials with Yield." *Journal of Rheology* 31: 385–404.

Paramane, S. B., and A. Sharma. 2008. "Consistent Implementation and Comparison of FOU, CD, SOU, and QUICK Convection Schemes on Square, Skew, Trapezoidal, and Triangular Lid-Driven Cavity Flow." *Numerical Heat Transfer, Part B (Fundamentals)* 54 (1-2): 84–102.

Pasquim, B. M., and V. C. Mariani. 2008. "Solutions for Incompressible Viscous Flow in a Triangular Cavity using Cartesian Grid Method." *Computer Modeling in Engineering and Sciences* 35 (2): 113–132.

Patankar, S. V., and D. B. Spalding. 1972. "A Calculation Procedure for Heat, Mass and Momentum Transfer in Three-Dimensional Parabolic Flows." *International Journal of Heat and Mass Transfer* 15 (10): 1787–1806.

Patil, D. V., K. N. Lakshmisha, and B. Rogg. 2006. "Lattice Boltzmann Simulation of Lid-Driven Flow in Deep Cavities." *Computers and Fluids* 35 (10): 1116–1125.

Peric, M., R. Kessler, and G. Scheuerer. 1988. "Comparison of Finite-Volume Numerical Methods with Staggered and Collocated Grids." *Computers and Fluids* 16 (4): 389–403.

Prashant, and Derksen, J. J.. 2011. "Direct Simulations of Spherical Particle Motion in Bingham Liquids." *Computers & Chemical Engineering* 35(7): 1200–1214.

Reddy, M. P., and J. N. Reddy. 1992. "Finite Element Analysis of Flows of Non-Newtonian Fluids in Three-Dimensional Enclosures." *International Journal of Non-Linear Mechanics* 27 (1): 9–26.

Sahin, M., and R. G. Owens. 2003. "A Novel Fully Implicit Finite Volume Method Applied to the Lid-Driven Cavity Problem-Part I: High Reynolds Number Flow Calculations." *International Journal for Numerical Methods in Fluids* 42 (1): 57–77.

Sanchez, F. J. 1998. "Application of a First-Order Operator Splitting Method to Bingham Fluid Flow Simulation". *Computers & Mathematics with Applications* 36 (3): 71–86.

Sanders, J., and E. Kandrot. 2010. *CUDA by Example – An Introduction to General Purpose GPU Programming* 1st ed.. Addison Wesley Professional. https://www.amazon.com/CUDA-Example-Introduction-General-Purpose-Programming/dp/0131387685

Sheu, T. W., and S. F. Tsai. 2002. "Flow Topology in a Steady Three-Dimensional Lid-Driven Cavity." *Computers and Fluids* 31 (8): 911–934.

Shinn, A. F. 2011. "Large Eddy Simulations of Turbulent Flows on Graphics Processing Units: Application to Film-Cooling Flows." Ph.D. thesis, University of Illinois at Urbana-Champaign, IL.

Shinn, A. F., M. A. Goodwin, and S. P. Vanka. 2009. "Immersed Boundary Computations of Shear-and Buoyancy-Driven Flows in Complex Enclosures." *International Journal of Heat and Mass Transfer* 52: 4082–4089.

Siegmann-Hegerfeld, T., S. Albensoeder, and H. C. Kuhlmann. 2013. "Three-Dimensional Flow in a Lid-Driven Cavity with Width-to-Height Ratio of 1.6." *Experiments in Fluids* 54 (6): 1–9.

Sundaresan, S., S. Nagarajan, S. M. Deshpande, and R. Narasimha. 1998. "2D Lid-Driven Cavity Flow at High Reynolds Numbers: Some Interesting Fluid-Dynamical Issues." In *Proceedings of the Sixteenth International Conference on Numerical Methods in Fluid Dynamics*, Vol. 515 of the series Lecture Notes in Physics, 231–236. Berlin/Heidelberg: Springer. http://link.springer.com/chapter/10.1007/BFb0106589

Syrakos, A., G. C. Georgiou, and A. N. Alexandrou. 2013. "Solution of the Square Lid-Driven Cavity Flow of a Bingham Plastic using the Finite Volume Method." *Journal of Non-Newtonian Fluid Mechanics* 195: 19–31.

Tang, X., Y. Su, F. Wang, and L. Li. 2013. "Numerical Research on Lid-Driven Cavity Flows Using a Three-Dimensional Lattice Boltzmann Model on Non-Uniform Meshes." *Science China Technological Sciences* 56 (9): 2178–2187.

Vanka, S. P. 2013. "2012 Freeman Scholar Lecture – Computational Fluid Dynamics on Graphical Processing Units." *ASME Journal of Fluids Engineering* 135 (6). doi:10.1115/1.4023858.

Vanka, S. P., A. F. Shinn, and K. C. Sahu. 2011. "Computational Fluid Dynamics Using Graphics Processing Units: Challenges and Opportunities." Proceedings of the ASME 2011 IMECE Conference, Denver, CO.

Verstappen, R., J. G. Wissink, W. Cazemier, and A. E. P. Veldman. 1994. "Direct Numerical Simulations of Turbulent Flow in a Driven Cavity." *Future Generation Computer Systems* 10 (2): 345–350.

Vola, D., L. Boscardin, and J. C. Latché. 2003. "Laminar Unsteady Flows of Bingham Fluids: A Numerical Strategy and Some Benchmark Results". *Journal of Computational Physics* 187 (2): 441–456.

Yapici, K., B. Karasozen, and Y. Uludag. 2009. "Finite Volume Simulation of Viscoelastic Laminar Flow in a Lid-Driven Cavity." *Journal of Non-Newtonian Fluid Mechanics* 164 (1): 51–65.

Yau, Y. H., A. Badarudin, and P. A. Rubini. 2012. “A Numerical Study of Secondary Flow and Large Eddies in a Driven Cavity.” *Journal of Mechanical Science and Technology* 26 (1): 93–102.

Yeckel, A., J. W. Smith, and J. J. Derby. 1997. “Parallel Finite Element Calculation of Flow in a Three-Dimensional Lid-Driven Cavity Using the CM-5 and T3D.” *International Journal for Numerical Methods in Fluids* 24 (12): 1449–1461.

Zhang, J. 2003. “Numerical Simulation of 2D Square Driven Cavity using Fourth-Order Compact Finite Difference Schemes.” *Computers and Mathematics with Applications* 45 (1-3): 43–52.